A Detector Upgrade for Phase-Imaging Ion Cyclotron Resonance Measurements at the CPT

by

Graeme Edward Baglow Morgan

A Thesis submitted to the Faculty of Graduate Studies of
The University of Manitoba
in partial fulfilment of the Requirements of the degree of

MASTER OF SCIENCE

Department of Physics and Astronomy
University of Manitoba
Winnipeg, Manitoba

Abstract

A position-sensitive microchannel plate (MCP) detector has been installed at the Canadian Penning Trap (CPT) mass spectrometer located at the CAlifornium Rare Isotope Breeder Upgrade (CARIBU) facility at Argonne National Laboratory in order to carry out Phase-Imaging Ion Cyclotron Resonance (PI-ICR) measurements. With this new measurement method, proof-of-principle mass measurements of five nuclei were made to a precision of $\delta m/m \approx 10^{-7}$. The PI-ICR results are found to be consistent with previous Time-of-Flight Ion Cyclotron Resonance (ToF-ICR) measurements. The content of this thesis covers the entire mass measurement process beginning with beam production at CARIBU through to ion detection at the CPT and a comparison of the ToF-ICR and PI-ICR measurement methods. The future of mass measurements at the CPT with this new technique will also be discussed.

Dedication

'When you can't run, you crawl.
When you can't crawl,
you find someone to carry you.'
-An old Browncoat saying

This thesis is dedicated to the many people who helped me up and kept me moving every time I felt like staying down.

Acknowledgements

First and foremost, I would like to thank my supervisor Kumar Sharma. His ability to illuminate how much more I needed to learn with elegance and humour kept me both continously motivated and humbled. If I continue in this field, I would hope to become a quarter of the scientist he is.

Secondly I wish to thank the leaders of the CPT group at Argonne, Jason Clark and Guy Savard. Jason for his infinite patience both in teaching me how to operate the experiment and in answering endless questions; Guy for always giving advice when it was needed even if it wasn't asked for, his ability to inspire us to greater efforts when things where not going well, and being willing to always have a laugh at how bad the Toronto Maple Leafs are.

Third, thanks must also go to the past and present students of the CPT group: Rodney Orford who learned the system along with me and contributed a great deal of his time into getting the new measurement system operational as well as educating me on the subject of craft beer; Shane Caldwell for many discussions on experimental methods, data analysis, and frisbee; Andrew Nystrom for carrying out several measurements at the CPT and aiding me in the data analysis process; Nancy Paul for helping to get the new detector up and running; and Mary Burkey for endless amounts of moral support.

Contents

List of Tables

List of Figures

1 Scientific Motivation for Mass Measurements of Short-Lived Neutron-Rich Nuclei

'My cruiser weighs 16,000 kilograms!'

-Trooper MacIntyre 'Mac' Womack

1.1 Penning Trap Mass Measurements

John R. Pierce first described the trapping of charged particles through the combination of a uniform magnetic field and electrostatic fields produced by hyperboloid-shaped electrodes [1]. This particle trap was first constructed by Hans Dehmelt who named the trap in honour of Frans M. Penning, inventor of a cold cathode vacuum gauge that used a combination of magnetic and electric fields with an ion discharge to measure vacuum pressures [2]. For his work concerning Penning traps, Dehmelt was awarded a share of the 1989 Nobel prize in physics [3].

The first mass measurement in a Penning trap occured in 1978 [4]. Nine years later at CERN, the Isotope Separation On-line Trap (ISOLTRAP) Penning trap carried out the first Penning trap mass measurements on radioactive species with five Rubidium isotopes and one Strontium isotope measured to an accuracy ($\delta m/m$) of at least 10^{-6} [5]. The successful ISOLTRAP measurements triggered a number of Penning trap experiments worldwide for use with radionuclides, including the Canadian Penning Trap (CPT) mass spectrometer involved in this work. Mass measurements are required for many fields of study such as nuclear structure, astrophysics, improvement of nuclear models and formulas, weak interaction studies, measurements of fundamental constants and more [6]. The required relative uncertainties for these fields of study are listed in table 1.1.

The mass measurements made at the CPT are intended for input into astrophysical calculations with a current focus on neutron-rich nuclides that are of importance to rapid neutron-capture process (r process) studies [7, 8].

Field of study	Required $\delta m/m$
General chemistry and nuclear physics	$10^{-5} - 10^{-6}$
Nuclear structure	$10^{-7} - 10^{-8}$
Astrophysics	10^{-7}
Nuclear models and formulas	$10^{-7} - 10^{-8}$
Weak interaction studies: CVC hypothesis, CKM unitarity	10^{-8}
Atomic physics: binding energies, QED	$10^{-9} - 10^{-11}$
Fundamental constants and symmetries	$\leq 10^{-10}$

Table 1.1: The required relative mass uncertainties for different fields of study. Adapted from [6].

1.2 The Astrophysical r Process

The synthesis of chemical elements in the universe is a fundamental scientific question that has yet to be completely answered. The light elements up to and including ^{7}Li are produced through big bang nucleosynthesis [9]. Progressing further, fusion reactions in stars are largely responsible for the formation of the elements up to ^{56}Fe [10]. For heavier nuclides, fusion is no longer energetically favourable and other processes must be responsible.

As can be seen in fig. 1.1, there are two separate sets of twin peaks for the solar abundances of the elements. The peaks at the atomic mass numbers $A = 138$ and $A = 208$ correspond to the intersection of the $N = 82$ and $N = 126$ neutron shell closures with the valley of stability, where the nuclei are particularly stable. The mechanism behind those two abundance peaks is the slow neutron-capture (s) process. In the s process, a nuclide captures neutrons on a timescale that is longer than most β decay lifetimes of the nuclides involved. After capturing a neutron, β decay pushes the nuclide to a higher Z along the valley of stability resulting in an eventual accumulation at a neutron shell closure.

The other set of peaks, at approximately $A = 130$ and $A = 195$, have no direct link between the neutron shell closures and stability. The responsible process is the rapid neutron-capture (r) process. The r process operates on the same principle as the $s$process, but much quicker as its name would suggest. During the duration of the r process, the neutron-capture rate is on a much smaller timescale than the β decay lifetimes and nuclides far from stability are produced. The accumulations occur again at the neutron shell closures, but at a lower Z compared to the s process as the nuclides were driven far from stability. This rapid neutron-capture process is thought to be responsible for the formation of almost half of the elements heavier than iron [10] as illustrated in fig. 1.1.

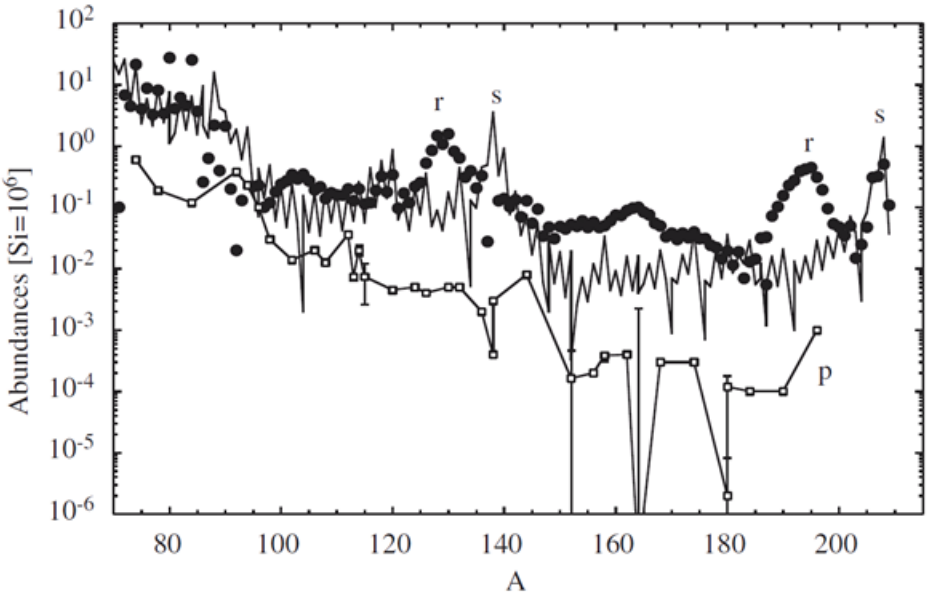

Figure 1.1: The solar abundances of heavy nuclides relative to Silicon with contributions labeled by nucleosynthesis process. The abundance peaks due to the r process occur at a lower mass number than the peaks due to the s process as they occur further from stability. Figure from [11].

In an environment with a high neutron density (greater than 10^{20} cm^{-3}) a seed nuclide will begin to rapidly capture neutrons through the reaction ${}^{A}_{Z}\mathrm{X}\ (n,\gamma)\ {}^{A+1}_{Z}\mathrm{X}$. As nuclides capture additional neutrons, increasingly neutron-rich nuclides will be produced. For such species,

the neutron separation energy S_n

$$S_n(Z,A) = \left[M(Z,A-1) + M_n - M(Z,A)\right] c^2. \tag{1.1}$$

as defined by eq. 1.1 will be comparatively lower.

If this environment also possesses a temperature on the order of 10^9 K, then the photodisintegration reaction, ${}^{A}_{Z}\mathrm{X}\ (\gamma, n)\ {}^{A-1}_{Z}\mathrm{X}$, opposes the neutron-capture. Since all nuclei in this region are unstable, β decay will push them to a higher proton number. The rates of these competing reactions dictate how the r process travels through the chart of the nuclides, referred to as the r process path. A visual example of the path is presented in fig. 1.2.

Provided that the environment has a suitably high temperature and the neutron-capture rates are sufficiently high, the competing reactions will reach an equilibrium within a given isotope chain. The point where this equilibrium occurs is referred to as a *waiting point* since the nuclide must wait for a β decay before the r process can continue.

At a waiting point, the relative yields of the two isotopes involved is given by the Saha equation [12]:

$$\frac{Y(Z,A+1)}{Y(Z,A)} = \frac{G(Z,A+1)}{2G(Z,A)} \left(\frac{A+1}{A}\frac{2\pi\hbar^2}{m_u kT}\right)^{3/2} n_n \exp\left(\frac{S_n(Z,A+1)}{kT}\right), \tag{1.2}$$

where $Y(Z,A)$ is the yield, $G(Z,A)$ the nuclear partition function, n_n the neutron number density, m_u the atomic mass unit, T the temperature, and S_n the neutron separation energy. In making the assumption of equivalent yields and partition functions along with the approximation of $A+1 \approx A$, eq. 1.2 can be solved for S_n at the waiting point,

$$S_n^0 = kT \ln\left[\frac{2}{n_n}\left(\frac{m_u kT}{2\pi\hbar^2}\right)^{3/2}\right]. \tag{1.3}$$

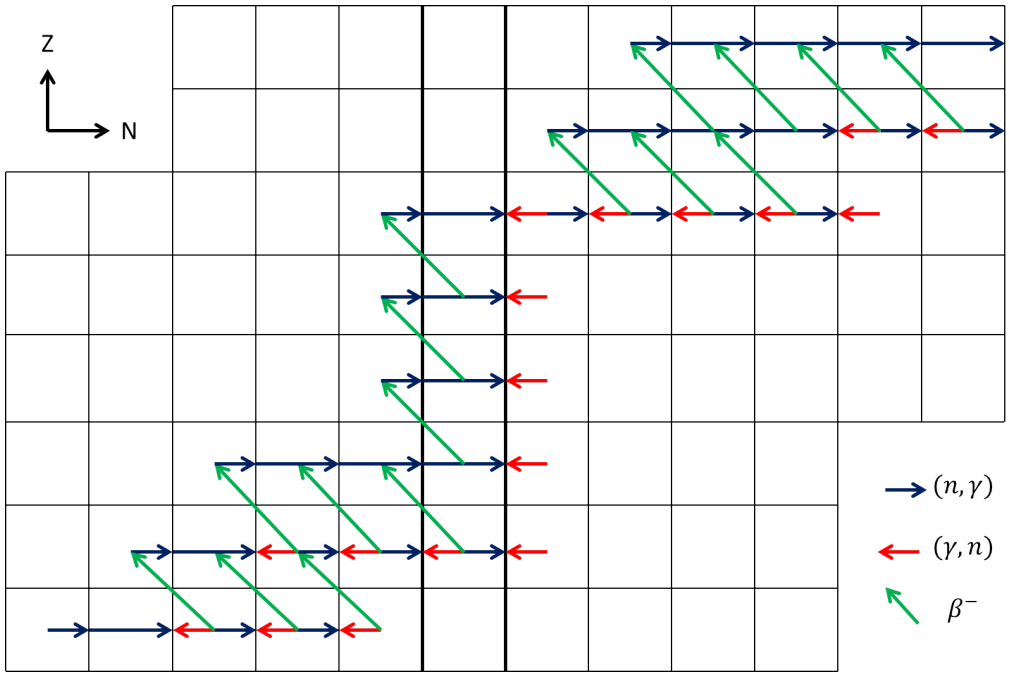

Figure 1.2: An example portion of an r process path. The three key processes, neutron-capture (n,γ), photodisintegration (γ,n), and β decay are represented with the blue, red, and green arrows respectively. The two darker black lines indicate a closed neutron shell. When the path crosses a closed neutron shell, the r process travels up the neutron shell until the neutron separation energies become large enough for the neutron-capture rates to outpace the photodissociation rates.

Due to even-odd pairing effects, this description is not wholly accurate as S_n sharply alternates with the addition of a neutron and it is a better choice to look at the two-neutron separation energy,

$$S_{2n}(Z,A+2) = S_n(Z,A+2) + S_n(Z,A+1) \approx 2S_n^0, \tag{1.4}$$

as the process will reach equilibrium at a nucleus of even N [13].

Adapting eq. 1.2 to the two neutron separation energy by multipying the ratios of $\frac{Y(Z,A+1)}{Y(Z,A)}$ and $\frac{Y(Z,A+2)}{Y(Z,A+1)}$ gives the expression

$$\frac{Y(Z,A+2)}{Y(Z,A)} = \frac{G(Z,A+2)}{G(Z,A)}\left(\frac{A+2}{A}\right)^{3/2}\left[\frac{n_n}{2}\left(\frac{2\pi\hbar^2}{m_u kT}\right)^{3/2}\right]^2 \exp\left(\frac{S_{2n}(Z,A+2)}{kT}\right). \tag{1.5}$$

In making the same assumptions as for eq. 1.3, S_{2n} is found to be

$$S_{2n} = 2kT\ln\left[\frac{2}{n_n}\left(\frac{m_u kT}{2\pi\hbar^2}\right)^{3/2}\right] \approx 2S_n^0. \tag{1.6}$$

From eq. 1.6, the separation energy at a waiting point can be calculated and a possible r process path can be described. Using assumed values of temperature and neutron density on the order of 10^9 K and 10^{24} cm^{-3} respectively gives a value of $S_n \approx 3.0$ MeV. This r process path can be illustrated through plotting the nuclides with a S_{2n} between 5.7 and 6.4 MeV as seen in fig. 1.3.

In terms of nuclear physics inputs for r process calculations, the neutron separation energy is the most important. The only direct measurements of this quanitity are mass measurements as shown in eq. 1.1.

The relative mass uncertainties of masses derived from experimental results from the 2012 Atomic Mass Evalution (2012 AME) [14] can be seen in fig. 1.3. In the region between the neutron shell closures of $N = 82$ and $N = 126$, there is a noticeable lack of reliable data on the neutron rich side of the valley of stability. Measurements of masses in this area with a relative uncertainty of 10^{-7} as stated by table 1.1 are desired for input into r process calculations like [15–17].

Unfortunately, the further one travels from stability the more difficult it becomes to carry out these mass measurements due to ever-shortening half-lives or the difficulty in producing the nuclides in sufficient quantity. In many cases the result is a wide gulf between nuclides whose masses have been measured to a suitable precision for astrophysical calculations and nuclides that are possible r process waiting points. To make up the difference, theoretical calculations are able to provide an estimate for these unknown masses. Providing input data for these mass models in the form of mass measurements far from stability is the most

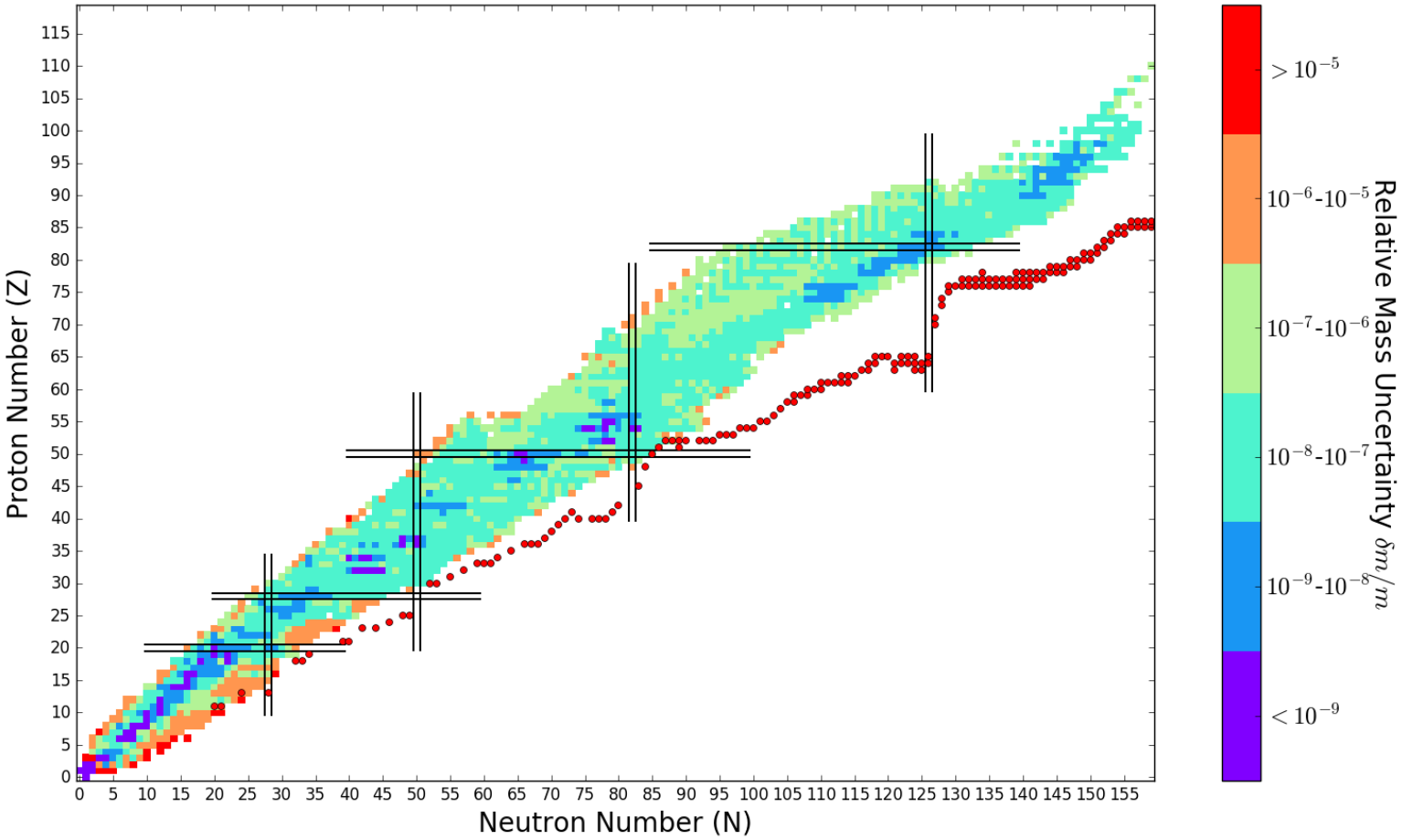

Figure 1.3: Relative uncertainty in masses derived from experimental results in the 2012 AME alongside a possible r process path. Magic numbers upwards from Z=20 and N=28 are highlighted.

efficient way to improve their overall accuracy. To illustrate this need, the mass excesses of cesium isotopes from several models relative to the FRDM95 [23] model along with the measured values from the 2012 AME are plotted in fig. 1.4.

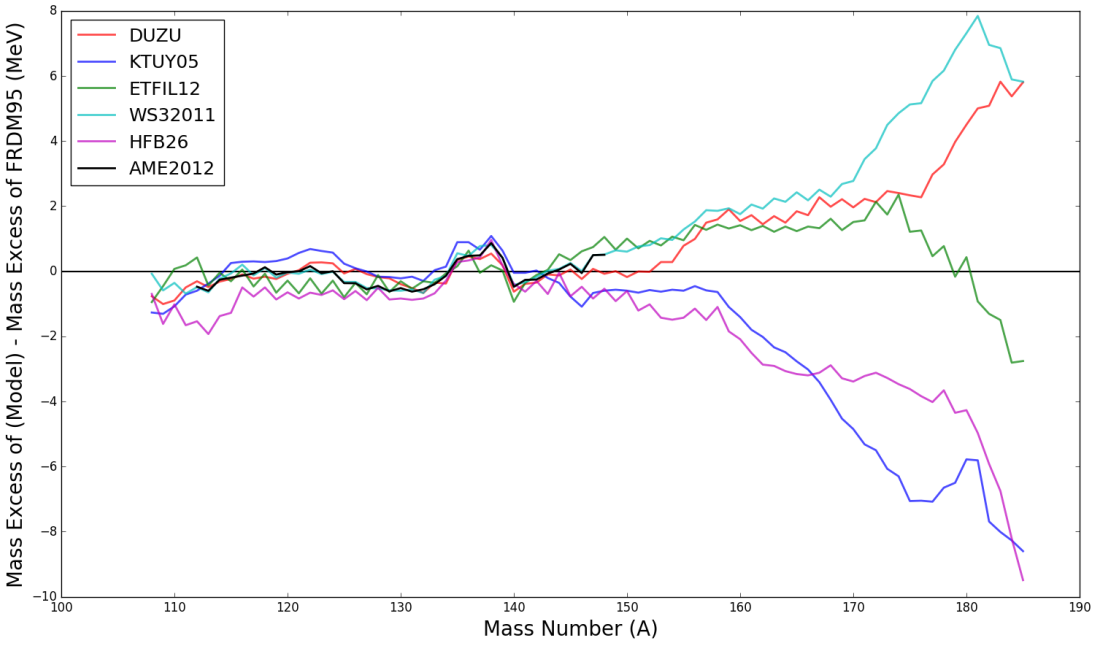

Figure 1.4: A comparison of the mass excess values from various mass models [18–22] and from the 2012 AME [14] for isotopes of Cesium. The reference model is the FRDM95 [23].

The mass models appear to be consistent and moderately accurate in the region of known masses, but begin to rapidly differ as isotopes get more neutron rich. Mass measurements of more neutron-rich nuclides are required to test the models, select reliable ones, and improve them.

In order to both improve mass models and provide input data for r process calculations, high-precision mass measurements of neutron-rich nuclei far from stability are needed. The CARIBU facility at Argonne National Laboratory is capable of providing nuclei in this region to the CPT mass spectrometer for mass measurements with a level of precision of at least 10^{-7}.

2 Ion Trapping

'Yeah, but...remember the part where it's a trap?'

-Hoban 'Wash' Washburne

In this section I will go over the confinement of ions through electromagnetic potentials in both two and three dimensions in two separate types of ion traps, namely the radio-frequency quadrupole (RFQ) or Paul trap and the Penning trap. The requirements for confinement and the ion motion in both cases will be discussed, followed by a derivation of the eigenmotions of ions in a Penning trap and two methods of manipulating the ion motion. The section will conclude with an examination of two different techniques for mass measurement with a Penning trap.

2.1 Radio-Frequency Quadrupoles

To confine a charged particle in a single dimension requires a restoring force in that dimension much like a mass tethered to a spring. For a particle possessing an electric charge of q and mass m, this restoring force is provided by the presence of an electrostatic field $\vec{E}$ acting in that dimension:

$$F_x = qE_x = -k_x(x - x_0) \tag{2.1}$$

where k_x is the restoring constant.

The electric potential V is given by $\vec{E} = -\nabla V$ which results in a potential for the one-dimensional case of

$$V = \frac{k_x}{2q}(x - x_0)^2 + V'. \tag{2.2}$$

The terms V' and x_0 are arbitrary constants and can be set to zero with no loss in generality.

To confine ions in two and three dimensions, the electric potential in one dimension can be generalized to

$$V = \frac{k_x}{2q}x^2 + \frac{k_y}{2q}y^2 + \frac{k_z}{2q}z^2. \tag{2.3}$$

Using Gauss's Law, $\nabla \cdot \vec{E} = \frac{\rho}{\epsilon_0}$, with a charge density $\rho = 0$, the potential must satisfy the Laplace equation $\nabla^2 V = 0$. The solution to the Laplace equation dictates that

$$k_x + k_y + k_z = 0. \tag{2.4}$$

In the two-dimensional case, the constant k_z is set to zero, and a trapping potential is obtained with the condition of $k_x = -k_y$. Combining this condition and choosing the magnitude of the potential to be $\frac{V_0}{2}$ at the position of $(x, y) = (r_0, 0)$ gives the trapping potential

$$V = \frac{V_0}{2r_0^2}(x^2 - y^2). \tag{2.5}$$

This potential can be produced by two sets of hyperbolic electrodes of opposite electrical potential $\frac{V_0}{2}$ oriented 90° with respect to each other with vertices of $(x, y) = (\pm r_0, 0)$ and $(x, y) = (0, \pm r_0)$ as in fig. 2.1.

With the potential V, the force on the ions is

$$\vec{F} = m(\ddot{x}\hat{x} + \ddot{y}\hat{y}) = q\vec{E} = -q\nabla V \tag{2.6}$$

$$= -\frac{qV_0}{r_0^2}(x\hat{x} - y\hat{y}). \tag{2.7}$$

The resulting equations of motion for the ions are

$$\ddot{x} = -\frac{qV_0}{mr_0^2}x \tag{2.8a}$$

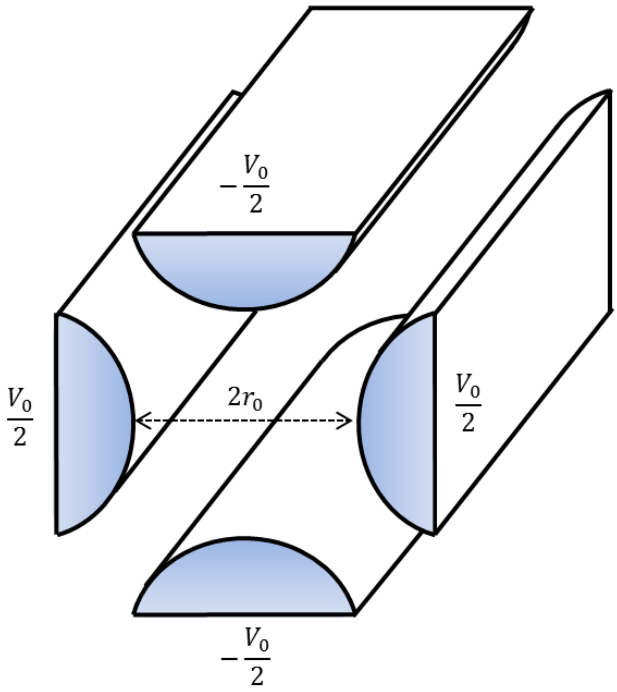

Figure 2.1: Hyperbolic electrode arrangement required to trap ions in two dimensions.

and

$$\ddot{y} = \frac{qV_0}{mr_0^2}y. \tag{2.8b}$$

From eqs. 2.8a and 2.8b, it can be seen that the ions in the trap are confined in the $\hat{x}$ direction and undergo simple harmonic motion with a frequency of $\omega = \sqrt{\frac{qV_0}{mr_0^2}}$ while the ions accelerate away from the origin in the $\hat{y}$ direction. The ions cannot be confined in both dimensions simultaneously.

This can be countered by making the applied potential a combination of a static component V_0' and a time-dependent component with a magnitude of V_1':

$$V_0 = V_0' + V_1' \cos(\omega t). \tag{2.9}$$

Now the confining force will alternate periodically and focus the ion within the electrodes.

This is known as an RFQ ion guide. The equations of motion now have the form

$$\ddot{x} = -\frac{q}{mr_0^2}(V_0' + V_1'\cos(\omega t))x \tag{2.10a}$$

and

$$\ddot{y} = \frac{q}{mr_0^2}(V_0' + V_1'\cos(\omega t))y. \tag{2.10b}$$

Making substitutions of

$$\eta = \frac{\omega t}{2} \qquad a = \frac{4qV_0'}{mr_0^2\omega^2} \qquad q' = \frac{2qV_1'}{mr_0^2\omega^2} \tag{2.11}$$

gives the equations of motion the form of the well-studied Mathieu equation:

$$\frac{d^2x}{d\eta^2} + (a + 2q'\cos(2\eta))x = 0 \tag{2.12a}$$

and

$$\frac{d^2y}{d\eta^2} - (a + 2q'\cos(2\eta))y = 0. \tag{2.12b}$$

For an analytical expression of the solution to the Mathieu equation and its use with respect to ion trapping see [24]. The physically pertinent solutions of the Mathieu equation are those in which the parameters a and q' produce either stable or unstable solutions [25]. For a stable solution the ion oscillates in the xy plane while it is free to move along the $\hat{z}$ direction, whereas for an unstable solution the ion is not confined within the plane and will be lost from the trap. A plot of the regions of stability for a and q' is shown in fig. 2.2.

The ratio of

$$\frac{a}{q'} = \frac{2V_0'}{V_1'} \tag{2.13}$$

is the operation line shown in fig. 2.2. The lower the slope of this line, the larger the

range of stable trajectories as the trap is stable between the q_{min} and q_{max} values. During operation, the values of V_0' and V_1' are fixed and make the mass-to-charge ratio of the ions in the trap the only variable that influences q' for a fixed frequency. The choice of the applied potentials V_0' and V_1' to the trap will then select the range of masses that will have stable trajectories.

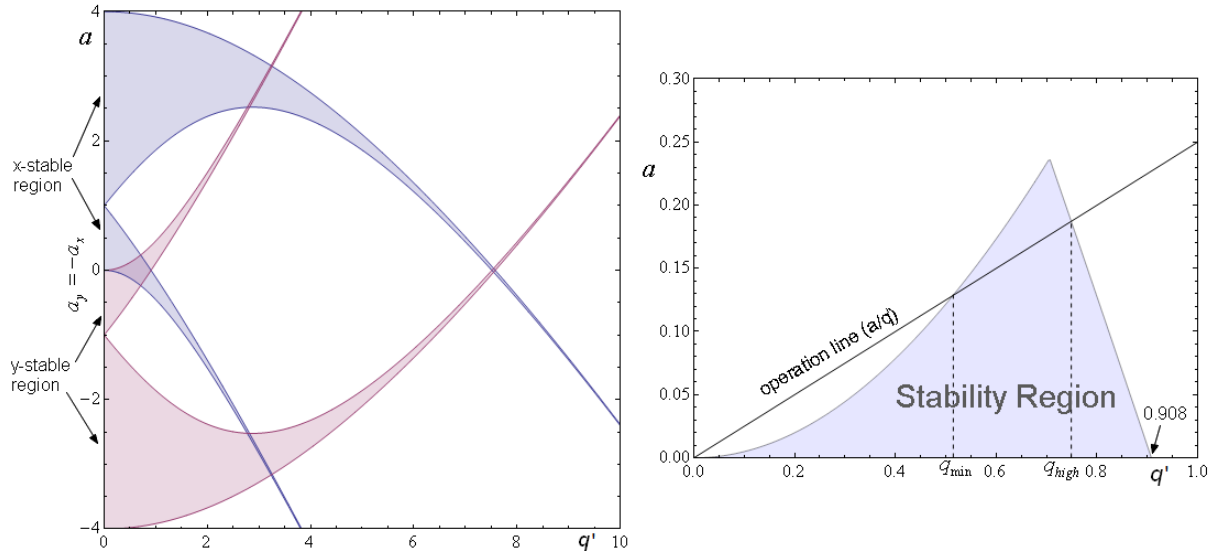

Figure 2.2: The regions of stability in a linear RFQ trap as defined by eqs. 2.12a and 2.12b. On the left, the blue and red shaded areas depict the regions of stability in $\hat{x}$ and $\hat{y}$ respectively. The ions are confined to the trap when the regions overlap. On the right, the blue shaded area represents the largest region of stability in both directions with an operation line of the trap parameters a and q'. Figure from [26].

One way of trapping ions in three dimensions with the RFQ ion guide requires segmenting the electrodes into three sections and applying a different value of V_0 such that the center section is at the potential minimum and the ions are confined. This configuration is used in the RFQ buncher at CARIBU and the Paul trap in the CPT system.

2.2 Penning Traps

In a homogenous magnetic field of magnitude B, a particle with charge q and mass m will be free to move along the direction of the field, but will be constrained to a circular orbit in the plane orthogonal to the field at the cyclotron frequency

$$\omega_c = \frac{qB}{m}. \tag{2.14}$$

Since the charged particle is not confined axially, the restoring force of an electrostatic field is required for confinement in three dimensions. Recalling eq. 2.4, a trapping potential in three dimensions can be obtained with the condition $k = k_x = k_y = -\frac{1}{2}k_z$. Converting to cylindrical coordinates gives a potential of the form

$$V = -\frac{k}{2q}(r^2 - 2z^2). \tag{2.15}$$

The constant $\frac{k}{2q}$ can be determined by defining a potential difference V_0

$$V_0 = V(0, z_0) - V(r_0, 0) = \frac{k}{2q}(r_0^2 + 2z_0^2), \tag{2.16}$$

and $\frac{k}{2q}$ is then

$$\frac{k}{2q} = \frac{V_0}{(r_0^2 + 2z_0^2)}. \tag{2.17}$$

The potential within the Penning trap can then be expressed as:

$$V = \frac{V_0}{2d^2}\left(z^2 - \frac{r^2}{2}\right) \qquad \text{with } d = \sqrt{\frac{1}{2}\left(\frac{r_0^2}{2} + z_0^2\right)}. \tag{2.18}$$

The electrodes needed to produce this potential are two end-cap electrodes in the shape of

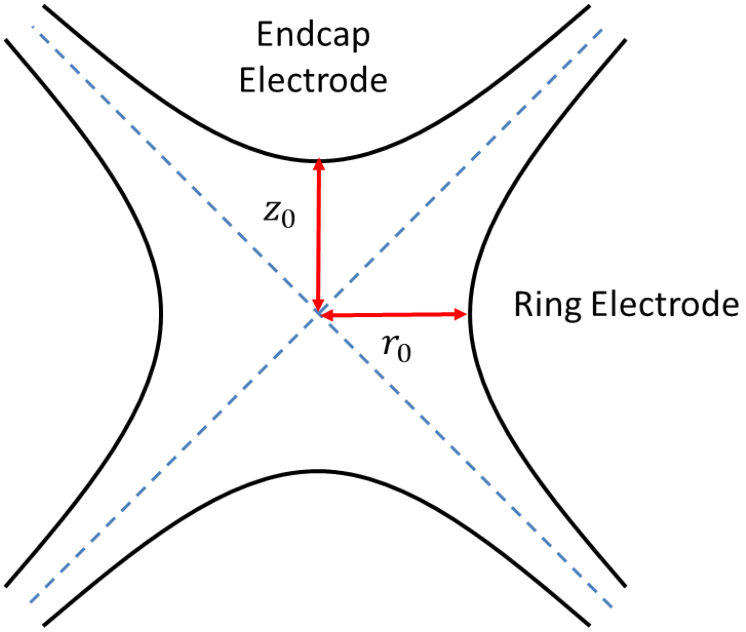

Figure 2.3: Cross-sectional view of the electrodes required to produce the potential of eq. 2.18.

infinite hyperbolas defined by

$$1 = \left(\frac{z}{z_0}\right)^2 - \left(\frac{r}{\sqrt{2}z_0}\right)^2 \tag{2.19}$$

and a ring electrode with an infinitely hyperbolic cross-section of

$$-1 = \left(\frac{z}{r_0/\sqrt{2}}\right)^2 - \left(\frac{r}{r_0}\right)^2. \tag{2.20}$$

A cross-sectional view of the hyperbolic electrodes is shown in fig. 2.3.

The force on an ion moving in the Penning trap is given by the Lorentz force:

$$\vec{F} = m\vec{a} = q(\vec{E} + \vec{v} \times \vec{B}). \tag{2.21}$$

Using eq. 2.18 and Gauss's Law, eq. 2.21 can be solved for the axial and radial equations of

motion [27]. The resulting differential equations in cartesian coordinates are

$$\ddot{z} = -\frac{qV_0}{md^2}z, \tag{2.22a}$$

$$\ddot{x} - \frac{qB}{m}\dot{y} - \frac{qV_0}{2md^2}x = 0, \tag{2.22b}$$

and

$$\ddot{y} + \frac{qB}{m}\dot{x} - \frac{qV_0}{2md^2}y = 0. \tag{2.22c}$$

From eq. 2.22a, it can be seen that the motion in the $\hat{z}$ direction is simple harmonic motion independent of the magnetic field with a frequency of

$$\omega_z = \sqrt{\frac{qV_0}{md^2}}. \tag{2.23}$$

As eqs. 2.22b and 2.22c are coupled, they can be simplified to a single second order differential equation with the substitution $u = x + iy$:

$$\ddot{u} + i\omega_c\dot{u} - \frac{\omega_z^2}{2}u = 0. \tag{2.24}$$

Solving this differential equation with the ansatz of $u = e^{-i\omega t}$ gives

$$\omega^2 - \omega_c\omega + \frac{\omega_z^2}{2} = 0, \tag{2.25}$$

with roots of the form

$$\omega_\pm = \frac{\omega_c}{2}\left(1 \pm \sqrt{1 - \frac{2{\omega_z}^2}{{\omega_c}^2}}\right). \tag{2.26}$$

The two roots in eq. 2.26 are commonly referred to as the reduced cyclotron (ω_+) and magnetron (ω_-) frequencies. They, along with ω_z, are the eigenfrequencies of motion for the

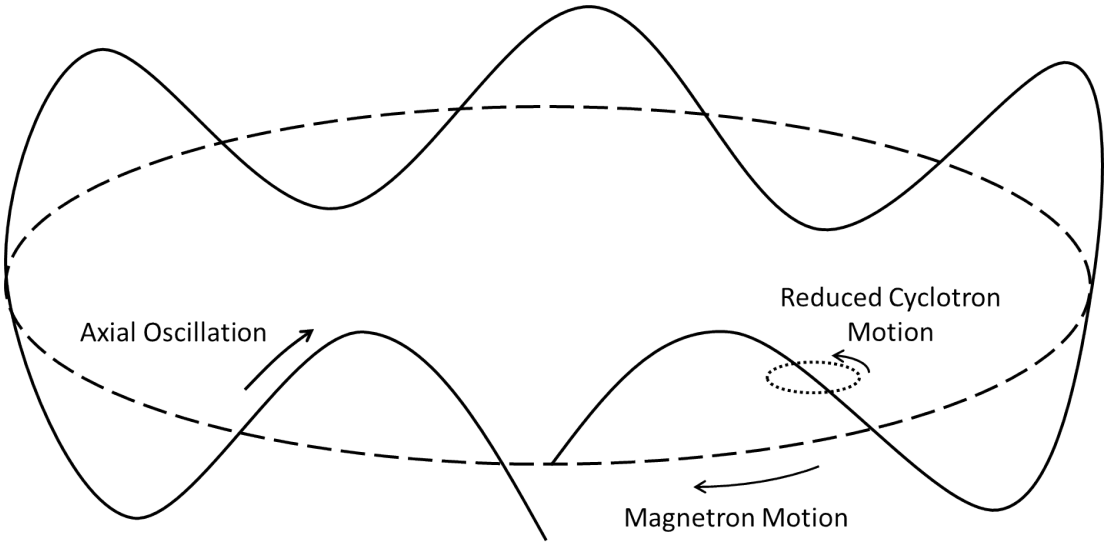

Figure 2.4: The motion of an ion in a Penning trap. Shown are the axial oscillation and the radial circular magnetron and reduced cyclotron motions.

trapped ion. Further examination of eq. 2.26 also yields the important relation of

$$\omega_c = \omega_+ + \omega_-. \tag{2.27}$$

In a typical Penning trap apparatus, the system parameters B, V_0, z_0, and r_0 are such that $\omega_+ \gg \omega_z \gg \omega_-$. This relation gives us the approximation of $\omega_c \approx \omega_+$ and allows ω_- to be Taylor-expanded, resulting in a mass independent magnetron frequency:

$$\omega_- \approx \frac{{\omega_z}^2}{2\omega_c} = \frac{2V_0}{B(2z_0^2 + r_0^2)}. \tag{2.28}$$

An illustration of the combined axial and radial motion of an ion in the Penning trap is depicted in fig. 2.4.

A more general solution of eq. 2.24 is the sum of the reduced cyclotron and magnetron solutions:

$$u = u_+ e^{-i\omega_+ t} + u_- e^{-i\omega_- t}. \tag{2.29}$$

Converting the general solution back to cartesian coordinates and making the substitution of $u_{\pm} = r_{\pm}e^{i\phi_{\pm}}$ gives the following radial motions of an ion in a Penning trap where r_+ and r_- are the respective amplitudes of the reduced cyclotron and magnetron motions:

$$x = r_+ \cos(\omega_+ t - \phi_+) + r_- \cos(\omega_- t - \phi_-) \tag{2.30a}$$

and

$$y = -r_+ \sin(\omega_+ t - \phi_+) - r_- \sin(\omega_- t - \phi_-), \tag{2.30b}$$

where ϕ_+ and ϕ_- are the initial phases of the ω_+ and ω_- and can both be set arbitrarily to zero.

2.3 Excitation of motion in a Penning Trap

With the application of an RF field, the motion of the ion inside the trap can be manipulated. If the applied frequency of the RF field is one of the eigenfrequencies of motion, then the motion in question is excited and the corresponding amplitude increases. To apply an RF potential on top of the required static potentials demands the separation of the hyperbolic ring electrode into equally sized segments.

2.3.1 Dipole Excitations

Applying a potential of the form

$$V_d = U_{rf} \cos(\omega_d t) x \tag{2.31}$$

to two opposite sections of the ring produces a dipolar RF field in the Penning trap and eq. 2.24 now becomes

$$\ddot{u} + i\omega_c\dot{u} - \frac{\omega_z^2}{2}u = -\frac{U_{rf}q}{m}\cos(\omega_d t). \tag{2.32}$$

In solving eq. 2.32, the amplitudes of the radial motions in eq. 2.30 are now time dependent:

$$x = r(t)_+ \cos(\omega_+ t) + r(t)_- \cos(\omega_- t), \tag{2.33a}$$

$$y = -r(t)_+ \sin(\omega_+ t) - r(t)_- \sin(\omega_- t). \tag{2.33b}$$

When the frequency of the dipole excitation, ω_d, is equal to $\omega_\pm$, energy is absorbed resonantly, and the radial amplitude increases by [28]

$$r_\pm(t) = r_\pm(0) + \frac{U_{rf}q}{2m(\omega_+ + \omega_-)}t. \tag{2.34}$$

As ω_+ is highly mass-dependent, an excitation at an ion's ω_+ frequency will act as a mass-selective filter by increasing the orbit of a particular species. Conversely, ω_- is approximately mass independent and will increase the orbit for all trapped particles.

2.3.2 Quadrupole Excitations

Another case is the application of a quadrupolar potential applied to a ring electrode segmented into four equal sections:

$$V_q = \frac{U_{rf}}{2a^2}\cos(\omega_q t)xy. \tag{2.35}$$

Like the dipole excitation, the amplitudes of eqs. 2.30 are now time dependent and have the

same form as eqs. 2.33:

$$r_{\pm}(t) = \left(r_{\pm}(0)\cos(\omega_b t) \mp \frac{r_{\pm}(0)(i(\omega_q - \omega_c)) + r_{\mp}(0)k_{\pm}}{2\omega_b}\sin(\omega_b t) \right) e^{-i\frac{(\omega_q-\omega_c)}{2}t}, \tag{2.36}$$

with

$$\omega_b = \frac{1}{2}\sqrt{(\omega_q - \omega_c)^2 + k_0^2}, \tag{2.37}$$

$$k_0 = \frac{qU_{rf}}{2ma^2(\omega_+ - \omega_-)}, \tag{2.38}$$

and

$$k_{\pm} = k_0 e^{\pm i\delta\phi}, \tag{2.39}$$

where ϕ is the phase of the applied frequency and is normally zero.

The amplitude of the radial kinetic energy of an ion in the trap is then

$$T_r(t) \propto \omega_+^2 r_+(t)^2 + \omega_-^2 r_-(t)^2 \approx \omega_+^2 r_+(t)^2. \tag{2.40}$$

For the quadrupole excitation when the applied frequency is the resonant ω_c, the radial amplitudes [29] are

$$r_{\pm}(t) = r_{\pm}(0)\cos\left(\frac{k_0 t}{2}\right) \mp r_{\mp}(0)e^{-i\Delta\phi}\sin\left(\frac{k_0 t}{2}\right). \tag{2.41}$$

In eq. 2.41, it can be seen that the radial amplitude oscillates between the magnetron and reduced cyclotron motion. The period of this motion is $t = \frac{2\pi}{k_0}$, giving a time of conversion from one to another of $t_{conv} = \frac{\pi}{k_0}$. In combination with the approximation of $\omega_c \approx \omega_+ \gg \omega_-$ and the time of conversion, eq. 2.38 can be rearranged to give the following relation between

the conversion time and the applied RF potential:

$$U_{rf} = 2a^2 B \frac{\pi}{t_{conv}}. \tag{2.42}$$

An illustration of this conversion can be seen in fig. 2.5.

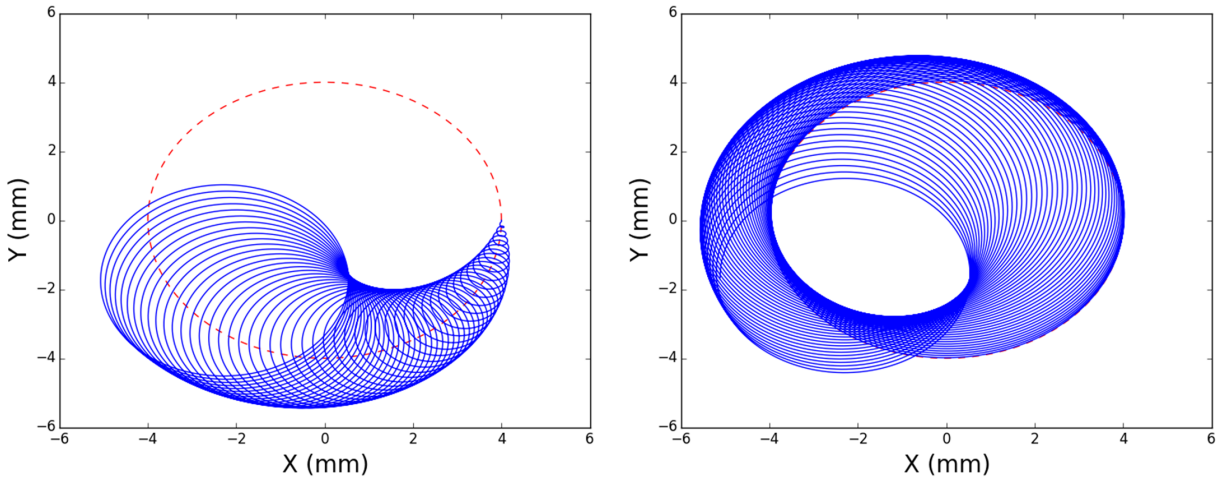

Figure 2.5: An illustration of the conversion of ω_- to ω_+ motion during a quadrupole excitation at the cyclotron frequency. The initial radius of the ω_- motion is represented by the dashed red line. The conversion is separated into two images for clarity.

For the off-resonant case where the applied frequency is not equal to the cyclotron frequency, the conversion of inital magnetron motion to reduced cyclotron motion is not complete and the change in radial kinetic energy will be less when compared to the resonant case. From eqs. 2.36 and 2.40, the radial kinetic energy for an ion that initially possessed magnetron motion would then be

$$T_r \propto \frac{\sin^2(\omega_b t_{conv})}{\omega_b^2}. \tag{2.43}$$

2.4 Time-of-Flight Ion Cyclotron Resonance

The time-of-flight ion cyclotron resonance (ToF-ICR) method of measurement is a technique for determining the eigenfrequencies of motion of a charged particle in the Penning trap by

recording the time of flight to a detector after ejection from the trap. The orbital magnetic moment of a charged particle that is exposed to an RF field is dependent on the frequency of said field through the gain in radial energy $T(\omega_{rf})$ from the excitation:

$$\vec{\mu}(\omega_{rf}) = \frac{T(\omega_{rf})}{B}\hat{z}. \tag{2.44}$$

The ejection of the charged particle from the trap results in the interaction between the orbital magnetic moment and the magnetic field gradient outside of the trap. The consequence is a force in the longitudinal direction and a conversion of the orbital kinetic energy to longitudinal energy:

$$\vec{F} = -\vec{\nabla}(\vec{\mu}(\omega_{rf}) \cdot \vec{B}) = -\mu(\omega_{rf})\frac{\partial B}{\partial z}\hat{z}. \tag{2.45}$$

As a result, a charged particle with a higher radial energy will have a shorter ToF and the resonant frequency from an excitation can be found. By successively exciting bunches of trapped ions and measuring their ToF over a range of excitation frequencies, a spectrum is created through plotting the average time of flight as a function of the excitation frequency. The minimum of this spectrum corresponds to the resonant frequency of the charged particle, ω_+ and ω_c for dipole and quadrupole excitations respectively.

Since the radial kinetic energy in eq. 2.43 is a sinc^2 function, the ToF spectrum will have the same form. The frequency resolution is the full width at half maximum (FWHM) of the central peak of the ToF spectrum. The line width $\Delta\nu(FWHM)$ for $t_{conv} = \frac{\pi}{k_0}$, when the initial magnetron motion is converted into reduced cyclotron motion, is obtained through a Taylor expansion of eq. 2.43 and is [29]

$$\Delta\nu(FWHM) \approx \frac{0.8}{t_{conv}}. \tag{2.46}$$

The importance of this relation cannot be overstated. The excitation time dictates the precision of a measurment through eq. 2.46 and the amplitude of the applied potential through eq. 2.42.

2.5 Phase-Imaging Ion Cyclotron Resonance

Phase-imaging ion cyclotron resonance (PI-ICR) is the process of determining the eigenfrequencies of motion through a measurement of the motion's phase, ϕ, accumulated after a period of no excitation. A position-sensitive detector is required in order to record the projection of the in-trap motion.

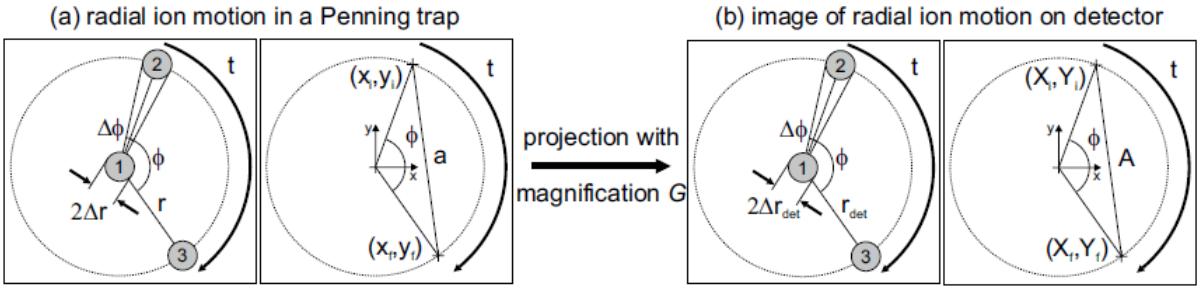

Figure 2.6: Positions of the ions throughout a PI-ICR measurement both in the trap (a) and projected onto a position-sensitive detector (b) with a magnification factor G. Positions 1,2, and 3 are respectively referred to as the center position, reference phase, and final phase. Figure from [31].

.

The general idea behind the measurement of ϕ is illustrated in fig. 2.6. Position 1 is the center of the trap where the ions are initially prepared for measurement possessing a spatial distribution of $2\Delta r$. With the application of a dipolar excitation at the frequency ω with a set initial phase, the ions are excited to a radius r labeled as position 2 and referred to as the reference phase. After a time t of no excitation, the ion motion has accumulated a phase of $\phi + 2\pi N = \omega t$ and is now at position 3, the final phase, with ϕ the angle between positions 2 and 3 and N the integer number of revolutions that occur in the time t. From

the measured phase ϕ, ω is calculated by

$$\omega = \frac{\phi + 2\pi N}{t}, \text{where} \begin{cases} \phi = \left|\arctan\left(\frac{Y_i}{X_i}\right) - \arctan\left(\frac{Y_f}{X_f}\right)\right| & 0 \leq \phi \leq \pi \\ \phi = 2\pi - \left|\arctan\left(\frac{Y_i}{X_i}\right) - \arctan\left(\frac{Y_f}{X_f}\right)\right| & \pi < \phi < 2\pi \end{cases} \tag{2.47}$$

where $X_{i,f}$ and $Y_{i,f}$ are the ideal projections on the detector of the in-trap positions $x_{i,f}$ and $y_{i,f}$ calculated with respect to the trap center, $(X \pm \Delta X, Y \pm \Delta Y) = G \cdot (x \pm \Delta x, y \pm \Delta y)$. The value N can be easily calculated given an approximate value of ω provided by a previous ToF-ICR measurement.

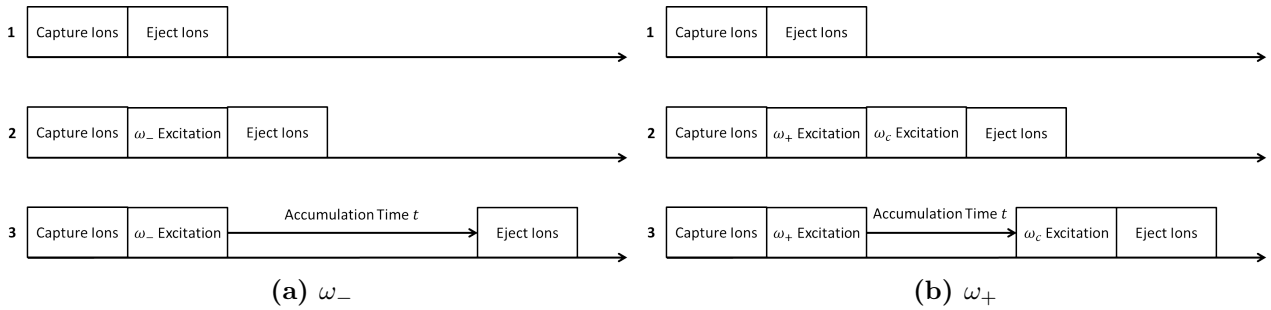

(a) ω_- **(b)** ω_+

Figure 2.7: Representation of the excitation schemes for the independent measurement of ω_- and ω_+.

For PI-ICR, there are two different excitation schemes depending on what frequency measurement is desired. In the first scheme, the magnetron or the reduced cyclotron frequency can be independently measured whereas in the second, a direct measurement of the cyclotron frequency is carried out [30]. No matter what frequency is being measured, the three general steps are the same:

1. The center is established through capturing and ejecting the ions from the trap without excitation.

2. The reference phase point is established from a dipolar excitation to set the ions on a ring of radius r followed by an ejection.

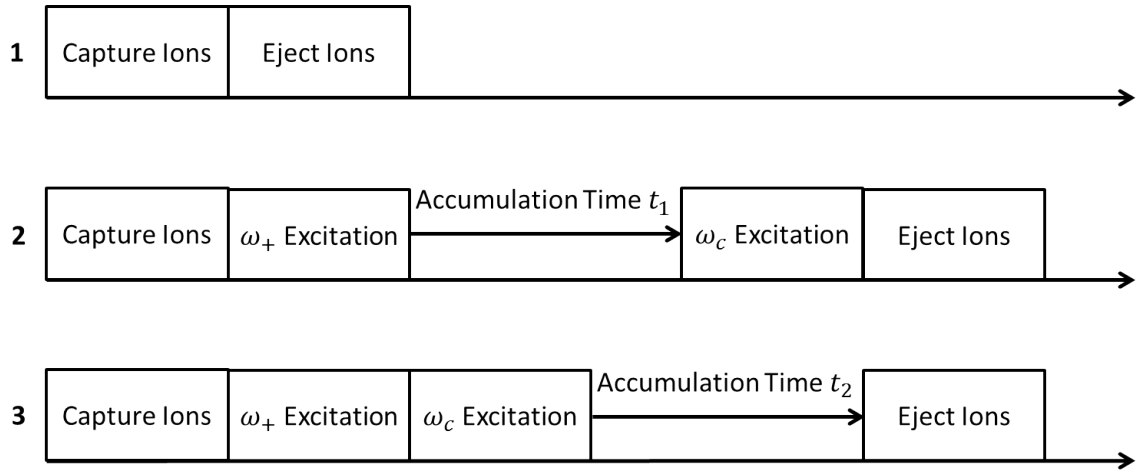

Figure 2.8: Representation of the excitation scheme for a direct ω_c measurement.

3. The final phase point is established from ejecting the ions following an accumulation time t after the initial dipolar excitation.

In ω_- and ω_+ measurements, as can be seen in fig. 2.7, the process is nearly identical except for a single additional step for the ω_+ measurement. Prior to ejection in steps 2 and 3, a quadrupolar excitation at ω_c converts the reduced cyclotron motion to magnetron motion. The purpose of this is to slow down the motion and prevent a significant angular spread of the projected image while preserving the phase change for the ω_+ motion [31].

For a direct ω_c measurement, step 2 is the same as step 3 for a ω_+ measurement as illustrated in fig. 2.8. The ions are excited by an ω_+ excitation and a phase corresponding to the reduced cyclotron motion, ϕ_+, is allowed to accumulate over a time t_1 before an ω_c excitation converts the motion prior to ejection giving $\phi_+ = \omega_+ t_1 + 2\pi N_+$. In step 3, the ω_c excitation immediately follows the ω_+ excitation, and a phase corresponding to the magnetron motion, ϕ_-, then accumulates over a time t_2 giving $\phi_- = \omega_- t_2 + 2\pi N_-$. If the accumulation times t_1 and t_2 are identical, then the angle ϕ between the reference and final images would be the phase change corresponding to $\omega_c = \omega_+ + \omega_-$:

$$\phi_c = \omega_c t - 2\pi(N_+ + N_-). \tag{2.48}$$

For PI-ICR measurements, the resolution is determined through the geometry of the phase images as in fig. 2.6:

$$\Delta\omega = \frac{\Delta\phi}{t} = \frac{\Delta k}{t\sqrt{1-k^2}}, \tag{2.49}$$

where $\phi = \arccos(k)$ for $0 \leq \phi < \pi$ and $\phi = 2\pi - \arccos(k)$ for $\pi < \phi < 2\pi$ and $k = (2r^2 - A^2)/(2r^2)$. As $\Delta\phi$ is a small angle, it is convenient to make the small angle approximation and eq. 2.49 can then be written as

$$\Delta\omega = \frac{\Delta\phi}{t} \approx \frac{2\Delta r}{tr}. \tag{2.50}$$

From eq. 2.50, the two parameters that dictate the resolution of the frequency measurement are the radial spread of the ions at positions 1-3 and the accumulation time t. The dependence of the resolution on the accumulation time is of great importance. The result is that the precision of the frequency measurement is dictated by the length of time that the experimenter can keep the ions in the trap.

3 Experimental Apparatus

'...I'm down with the capital C-P-T'

-Ice Cube

In this section, I will go over the entirety of the experimental system starting with the components that form CARIBU and the production of the beam from ^{252}Cf fission products. Following will be an overview of the CPT system detailing the path the ions take to the Penning trap. Finally, the procedure for both mass measurement techniques used at the CPT and methods for analyzing the recorded data will be covered.

3.1 CARIBU

The CAlifornium Rare Isotope Breeder Upgrade (CARIBU) facilty is located at Argonne National Lab (ANL) and was built to provide neutron-rich radioactive beams to be delivered to experimental areas served by the Argonne Tandem Linac Accelerator System (ATLAS). At CARIBU, the spontaneous fission fragments of a Californium-252 radioactive source are thermalized and extracted to form a beam that can be then transported to an experiment. The layout of the CARIBU facility is displayed in fig. 3.1. A more detailed description of CARIBU can be found in the recent doctoral theses of Jonathon Van Schelt [32] and Daniel Lascar [33].

3.1.1 ^{252}Cf Ion Source

The source providing the neutron-rich nuclei for CARIBU is a sample of ^{252}Cf deposited onto a stainless steel plate, covered by a gold foil approximately 1 mg/cm^2 thick, located at the back of a gas cell that is commonly referred to as a gas catcher by the CPT collaboration.

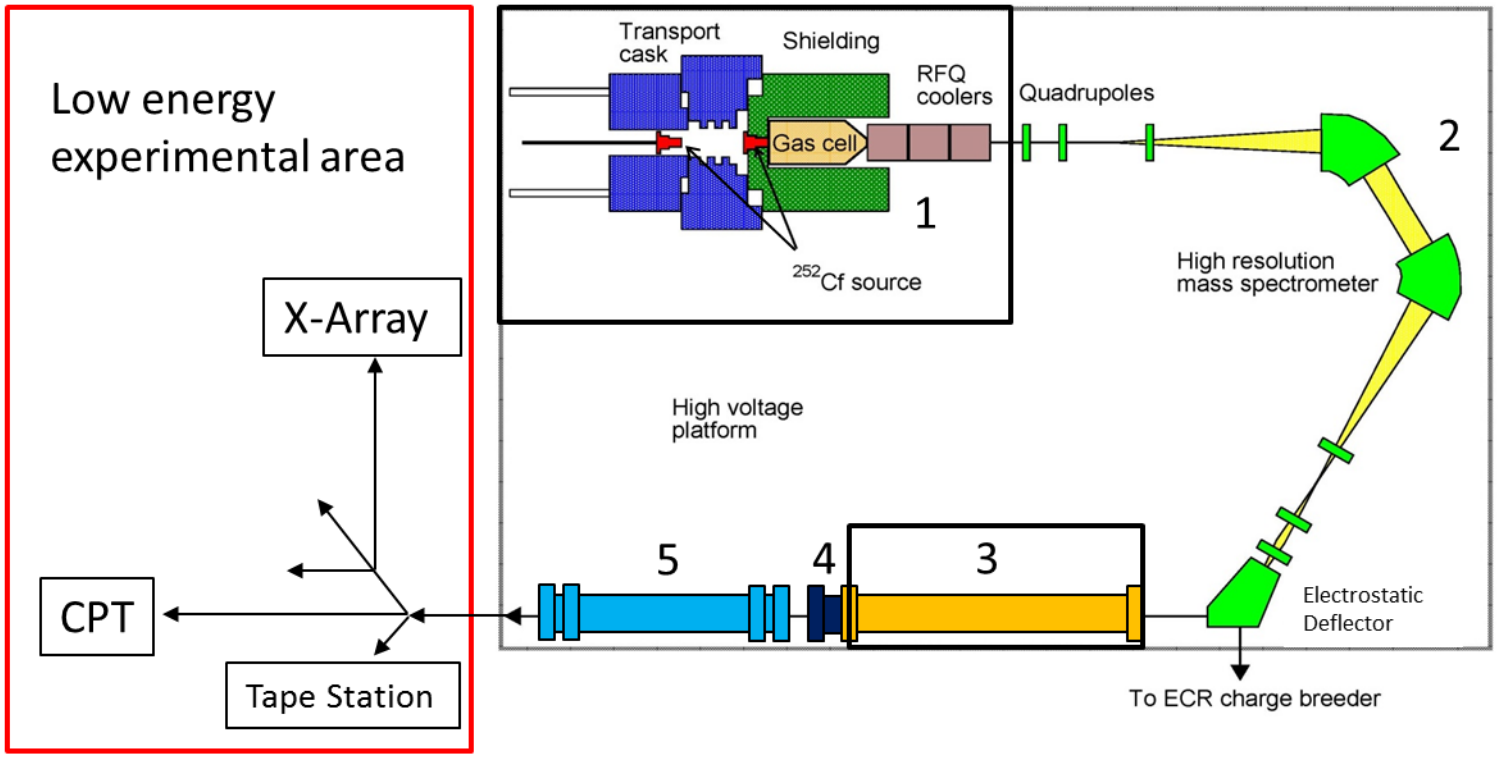

Figure 3.1: Layout of the CARIBU facility. Shown are the ^{252}Cf source (shown in both the retracted and inserted positions) and gas cell (1), the isobar separator (2), the RFQ buncher (3), the elevator (4). the Multi-Reflection Time-of-Flight mass separator (MR-ToF) (5), and the low energy experimental area.

The source was produced at Oak Ridge National Laboratory with a measured strength of 1.7 Ci as of Fall 2013.

^{252}Cf has a half-life of 2.645(8) years, decaying via α decay with a 96.908(8)% probability and via spontaneous fission the remaining 3.092(8)% [34]. As seen in fig. 3.2, the fission products of ^{252}Cf are distributed around two peaks located at approximately A=100 and A=140. The production of such a large assortment of neutron-rich nuclei make a ^{252}Cf fission source ideal for r process motivated measurements in this region. As the source emittance is isotropic, the forward-facing half of the fission fragments produced enter the CARIBU gas catcher.

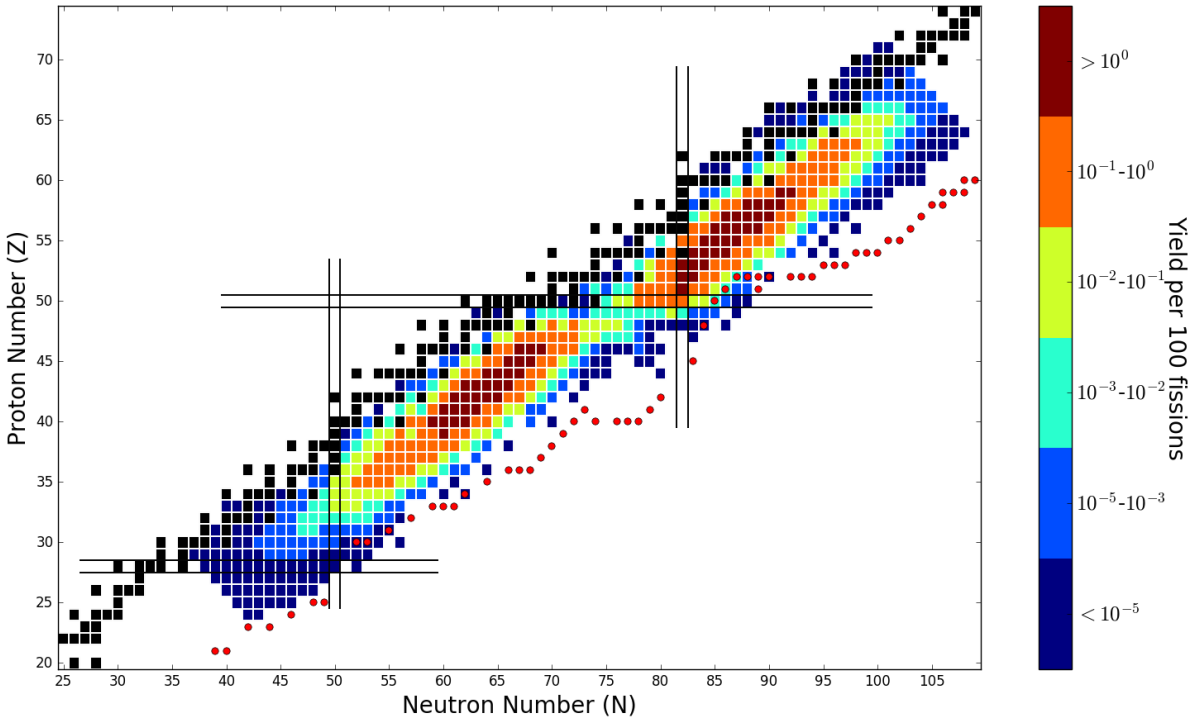

Figure 3.2: The yield of ^{252}Cf per 100 fissions overlaid onto the chart of nuclides. The stable nuclides are represented by black squares and magic numbers in this area are highlighted. A possible r process path is shown by the red data points. Fission yield values are taken from [35].

3.1.2 Gas Catcher

The lynchpin of CARIBU is the large volume gas catcher. The first gas catcher system was developed at ANL in 1998 as a means to provide radioactive ions for the CPT [36]. The purpose of the gas catcher is to thermalize the forward scattering fission fragments and focus them so they can be extracted from the gas catcher and formed into a radioactive beam.

Two main sections compose the gas catcher, a cylindrical body and a cone. The fission fragments enter the body after passing through a degrader foil of 2 mg/cm^2 aluminum that is meant to remove the majority of a fragment's kinetic energy. The interior of the gas catcher is filled with high-purity Helium gas. This slows and thermalizes the fission fragments. A DC gradient along the length of the gas catcher combined with an RF focusing field is applied to the electrodes that comprise each section. The gas flow and the DC gradient move the ions through the length of the gas catcher to the extraction nozzle at the end of the cone while the RF field focuses the ions along the central axis and away from the walls.

Upon exit from the gas catcher, the ions enter a series of RFQ ion guides where the remaining Helium gas is removed through differential pumping. The cooled and collimated beam is then accelerated to an energy of up to 36 keV/e through a set of acceleration electrodes. To achieve this, the gas catcher is positioned in an electrically isolated cage that is biased 36 kV above the CARIBU platform. The accelerated beam is now ready for in-flight mass separation at the isobar separator.

3.1.3 Isobar Separator

Designed to fit on the CARIBU platform, the isobar separator is made of two 60° bending magnets interspersed with a 48-pole electrostatic correction lens in order to correct for aber-

rations. The observed mass resolution with a 36 keV beam is typically 1/9000. After the isobar separator, the beam is directed towards the low-energy experimental beamline by an electrostatic deflector.

3.1.4 RFQ Buncher

After the beam is deflected into the low-energy experimental beamline, it enters the RFQ buncher. The buncher is a linear RFQ ion-guide filled to a typical pressure of 10^{-5} Torr with high-purity Helium gas. Forty-nine quadrupole segments make up the buncher with the final three electrodes forming the trap that accumulates the continuous beam from CARIBU [33]. The trap in the buncher is opened periodically, typically every 100 ms, and a discrete bunch of ions is sent to the experimental area. As the ions approach the buncher at energies 36 keV/e, the buncher is held inside an electrically isolated cage that is held at the same potential as the gas catcher cage. Holding the buncher at the same potential as the gas catcher is necessary in order the trap the beam. The result is a bunched beam leaving the buncher with energies of 36 keV/e.

Since the CPT is operated near ground, the energy of the ion beam needs to be lowered to a manageble level. This is done through an electrostatic elevator consisting of an electrically isolated drift tube that is pulsed from the gas catcher potential to approximately 2 kV while ion bunches are inside the tube.

3.1.5 MR-ToF

The bunched beam subsequently enters the Multi-Reflection Time-of-Flight (MR-ToF) mass separator. The MR-ToF was installed in December 2014 at CARIBU and has been recently commissioned. When not in use, the MR-ToF functions as a drift tube section allowing the beam from CARIBU to be delivered to the CPT and other experimental stations in the

low-energy experimental area in CARIBU. The MR-ToF was not used in this work as it was not operating when the measurements in section 4.2.2 were taken.

The purpose of the MR-ToF is to provide a higher level of isobar purification than that initially provided by the isobar separator. It consists of two electrostatic ion-optical mirrors on either end of a drift electrode as illustrated in fig. 3.3. To trap an ion bunch leaving the RFQ buncher, the drift section potential is lowered with the ion bunch inside. The ion bunch is then reflected repeatedly between the two electrostatic mirrors. The different species present in the ion bunch leave the RFQ Buncher with a given potential V and gain a kinetic energy of

$$T = qV = \frac{m_i v_i^2}{2}. \tag{3.1}$$

Since each species in the ion bunch possesses a unique charge-to-mass ratio, each will possess a unique velocity. The result is a species dependent time of flight in the drift section between the electrostatic mirrors [37]. In each pass between the mirrors, the difference in time of flight increases giving a mass-dependent separation.

Eventually the separation between species is larger than the time width of each species-specific ion bunch and at this point the potential of the drift section is raised to allow the ions to exit. Following the second electrostatic mirror is a grid of wires orthogonal to the beam known as a Bradbury-Nielsen gate. The deflection voltage applied at the gate is then dropped for a short interval to only allow the ion bunch of interest to pass while all other bunches are deflected [38].

The CARIBU MR-ToF is modelled after the MR-ToF at the ISOLTRAP experiment. The ISOLTRAP MR-ToF possesses a maximum mass resolution of approximately 1/200000 accomplished over a cycle time of 30 ms [39]. The maximum projected mass resolution to be provided by the CARIBU MR-ToF is expected to be similar, but the short lifetimes of exotic isotopes may necessitate a compromise on mass resolution in order to have adequate time

to perform a measurement at the Penning trap.

After leaving the MR-ToF, the bunched and purified beam is made available to the installed experiments in the low-energy experimental area.

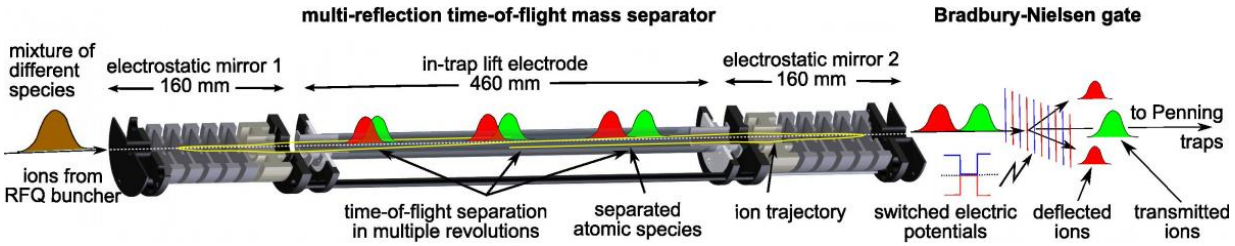

Figure 3.3: Illustration of the MR-ToF method of operation. Ion species are represented by the coloured Gaussian-shaped distributions. Figure from [39].

3.2 Canadian Penning Trap System

The key component of the Canadian Penning Trap System is the CPT, which is located inside the bore of a 5.7 T superconducting magnet at the top of a tower in the low-energy experimental area in CARIBU as can be seen in fig. 3.4. The bunched, low-energy beam taken from CARIBU is transferred to the Penning trap for measurement. In the following subsections the relevant components of the tower, the Penning trap, and the measurement procedures for both the ToF-ICR and PI-ICR methods will be covered.

3.2.1 Stable Ion Source

In the transfer line prior to the 90° deflector on fig. 3.4 there is a stable ion source (SIS) for calibrating the system. The SIS is a ^{133}Cs surface ionization source that emits $^{133}Cs^{+}$ ions via thermionic emission that get injected into the CPT tower through a set of accelerating electrodes and a 90° deflector. Besides using the SIS to tune the tower components in order to maximize transmission, the $^{133}Cs^{+}$ ions are also a good choice as a calibrant frequency for cyclotron frequency measurements due to their stability and precisely known mass.

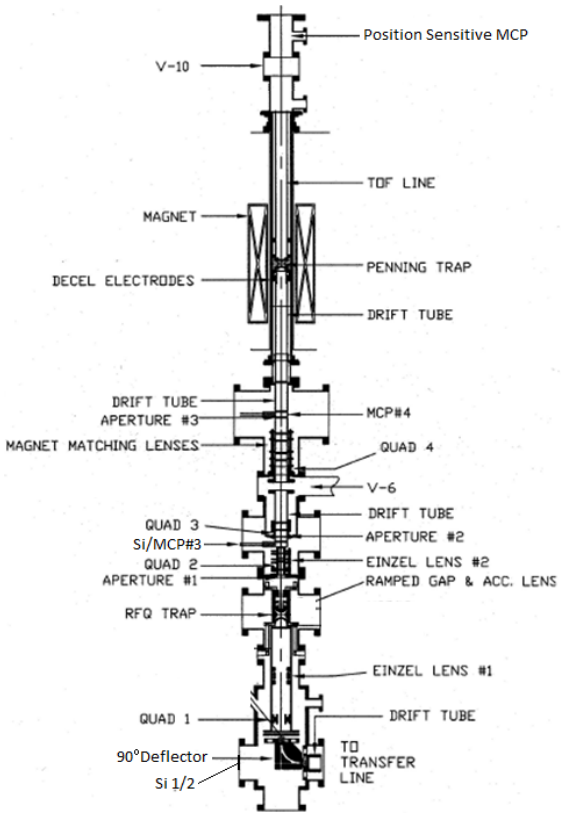

Figure 3.4: A schematic of the CPT tower from the 90° deflector to the position-sensitive MCP detector. Labelled are the RFQ Paul Trap, the Penning trap, the ToF line, all focusing and steering elements, and all diagnostic silicon and MCP detectors.

3.2.2 Paul Trap

Downstream of the cross that holds the SIS is the first diagnostic station to tune transmission from CARIBU. It is referred to as Si/MCP 0 as both a silicon surface barrier detector and a microchannel plate detector are available. Following the diagnostic section is an electrostatic elevator much like the one at CARIBU that brings the ions down to the ground potential of the tower as they leave CARIBU with energies of approximately 2 keV/e. If desired, the deflector after the elevator can be set at drift potential to allow the ions to travel straight through to another diagnostic detector, Si 1/2. Exiting the elevator, the ions are sent up the tower via the 90° deflector and through the quadrupole steerer, Quad 1, and the first einzel lens prior to entering the RFQ Paul trap.

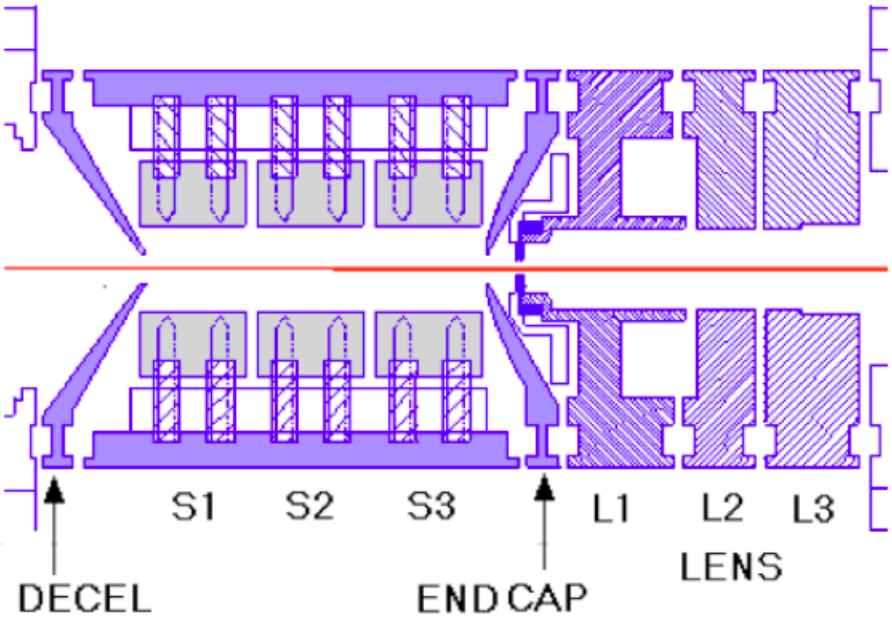

Figure 3.5: Schematic of the Paul trap and subsequent acceleration electrodes.

Electrode	Capture (V)	Trap (V)	Eject (V)
Decel	7.7	19.7	19.7
S1	−5.8	6.2	31.2
S2	−6.9	−6.9	−6.9
S3	6.2	6.2	−48.8
Endcap	19.7	19.7	−35.3

Table 3.1: Electrode biases of the Paul trap throughout the capture/trap/eject cycle.

In the Paul trap, the ion bunches from CARIBU are accumulated and thermalized by the introduction of high purity Helium gas at liquid Nitrogen temperatures in preparation for measurement at the Penning trap. The cooling of the Paul trap is done by recirculating liquid Nitrogen through a jacket in thermal contact with the trap. The electrode biases throughout the capture/trap/eject cycle are listed in Table 3.1.

The ion bunches ejected from the Paul trap encounter the second set of steerers, a lens, and another diagnostic station labeled Si/MCP 3. Si/MCP 3 sees the most use out of all diagnostics as it is best situated to tune the Paul trap voltages and pulse timings in order to maximize transmission of the cooled ion bunches to the upper half of the CPT tower. After the diagnostic station, the ions pass through a third set of steerers and enter the upper half

of the tower where the Penning trap is located.

3.2.3 Penning Trap

The ions enounter one last set of steerers and the magnet matching lens before MCP 4, the final diagnostic detector. Past MCP 4 is the drift tube leading to the key component of experimental apparatus, the Penning trap. The Penning trap is comprised of seven electrodes as shown in fig. 3.6. The ring electrode is divided into four equal sections to allow both dipole and quadrupole excitations and, along with both endcap electrodes, possesses the hyperbolic shape required to produce the trapping potential. The correction rings and tubes are used to compensate the changes to the ideal trapping potential brought on by the finite size of the electrodes and the required apertures to allow ions to enter and leave. The biases of the Penning trap electrodes throughout a measurement cycle are listed in table 3.2.

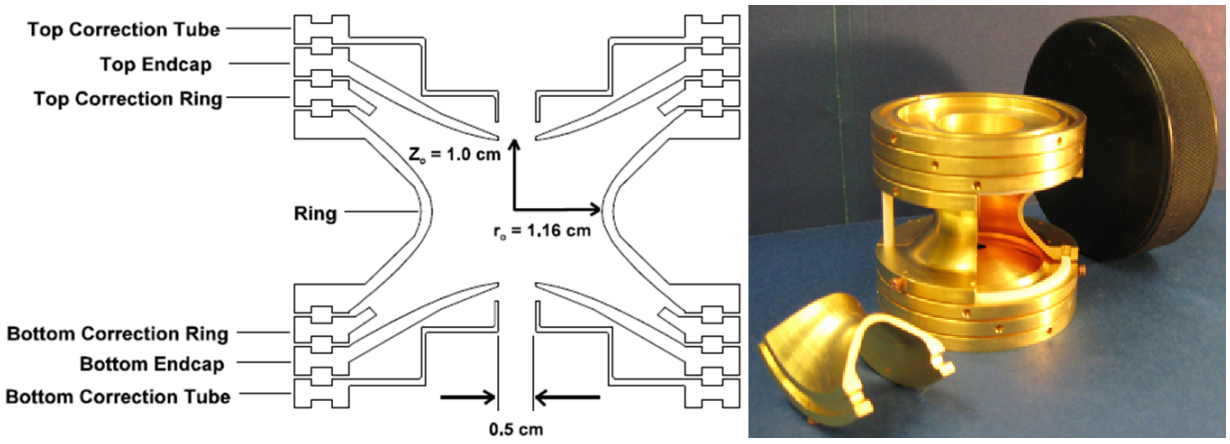

Figure 3.6: On the left is a schematic of the Penning trap electrodes with the aperture size and trap dimensions defined. On the right is a picture of the Penning trap with a hockey puck for scale.

After spending the requisite amount of time in the Penning trap, the ion bunches are ejected and make their way through the ToF line to the final MCP detector. The ToF line is a set of nine electrodes labeled ToF A through to ToF I, that accelerate and focus the ions towards the detector. ToF A is the longest as the ions see the largest shift in magnetic field over

Electrode	Capture (V)	Trap (V)	Eject (V)
Bottom Correction Tube	−4.53	0.47	0.47
Bottom Endcap	−7.24	−3.24	−3.24
Bottom Correction Ring	−7.99	−7.99	−7.99
Ring	−13.45	−13.45	−13.45
Top Correction Ring	−7.99	−7.99	−7.99
Top Endcap	−3.24	−3.24	−13.24
Top Correction Tube	0.47	0.47	−14.53

Table 3.2: Electrode biases of the Penning trap throughout the capture/trap/eject measurement cycle.

that distance with the resulting change from radial to axial energy. It is held at a potential slightly below the Penning trap ejection potential to allow the ions to drift slowly enabling the conversion to take place effectively. For ToF-ICR measurements the voltages settings past ToF A form an ion-optical system that directs the ions to the detector, whereas for PI-ICR the biases are set to quickly extract the ions and keep the ToF distribution between the trap and the detector as narrow as possible [30]. The stress ring H and I electrodes compensate for the gap required to fit a valve between ToF H and I. Pictures of the Penning trap with the ToF along with a schematic outline are shown in fig. 3.7. The ToF line electrode biases used in this work are listed in table 3.3.

Electrode:	A	B	C	D	E	F	G	H	I	H/I Stress
ToF-ICR Bias (V):	-16	-100	-250	-500	-400	-800	-140	-800	-800	-800
PI-ICR Bias(V):	-35	-400	-400	-400	-400	-400	-400	-400	-400	-400

Table 3.3: Electrode biases of the ToF line from the Penning trap to the MCP for each method of measurement.

The MCP detector used at the CPT is a RoentDek DLD40 with a delay line anode, fig. 3.8. It has an active diameter of 45 mm, a position resolution of < 0.1 mm, and a dead time of 10-20 ns [41]. A pair of matched microchannel plates are stacked in chevron configuration with a potential of -2400 V applied across and are mounted in front of the anode structure. The anode wire array consists of two helical pairs of delay lines, a signal wire and a reference wire for each dimension. The charge cloud emitted from the plates due to an ion hit strikes

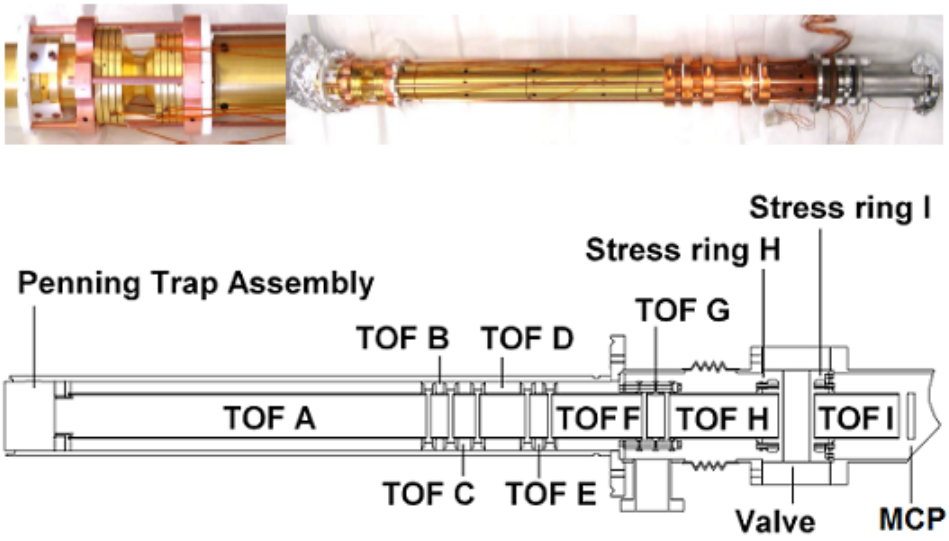

Figure 3.7: In the upper left is a picture of the deceleration electrodes, the Penning trap, and ToF A. In the upper right is the Penning trap with ToF A-H. Below the pictures is a schematic of the ToF electrodes. Pictures from [32] and figure adapted from [40].

the delay lines and the signal propagates through the signal wires in each dimension, as illustrated in fig. 3.9. The position of the ion hit on the MCP in either dimension is proportional to the difference in the time taken for the signal to hit each end of a wire. Five signals are read from the detector: x_1, x_2, y_1, y_2, and the signal from the initial ion hit on the MCP that is used as the timing reference for the other four signals. This new detector was installed in December 2014 and replaced the previous detector, a DeTech model 402A-H channel electron multiplier, in order to make PI-ICR measurements possible.

In order to install the MCP detector in the chamber that housed the previous detector, a custom mounting flange was designed as part of this work. A blank zero-length ConFlat flange was modified with a hole in the center and four bolt holes intended for the stand-off rods to hold the mounting ring. The stainless steel mounting ring has two sets of four bolt holes, one set for the stand-off rods from the modified flange and the other for accommodating the four threaded rods on the detector's anode structure. Eight alumina hat washers electrically isolate the detector from the mounting ring.

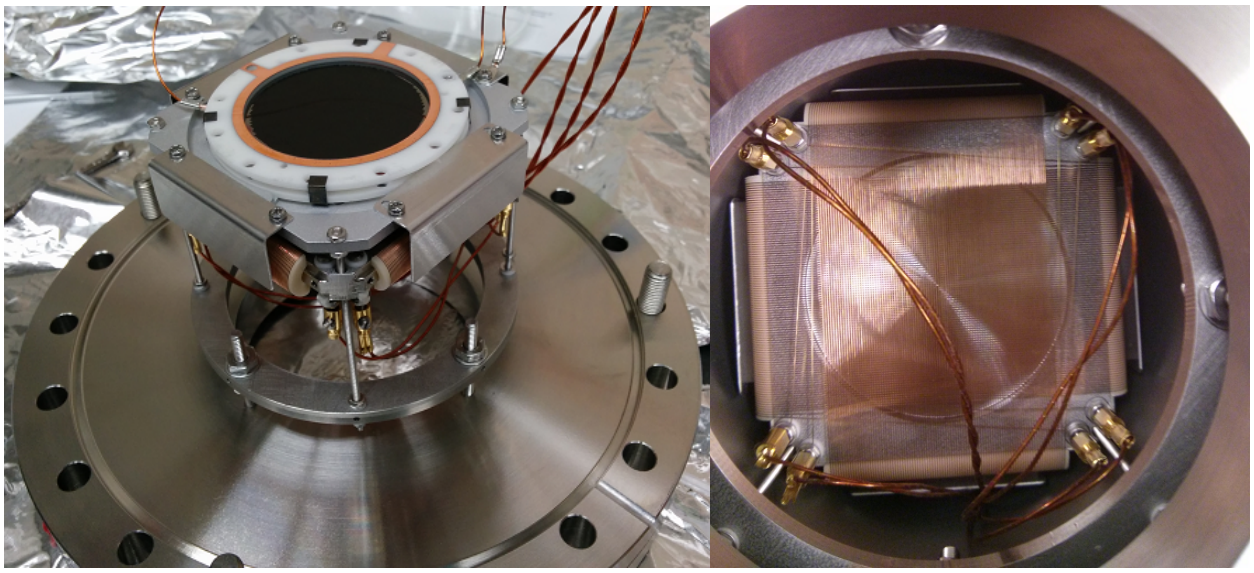

(a) **(b)**

Figure 3.8: The Roentdek DLD40 MCP detector (a) on its mounting flange and the delay lines of the anode (b).

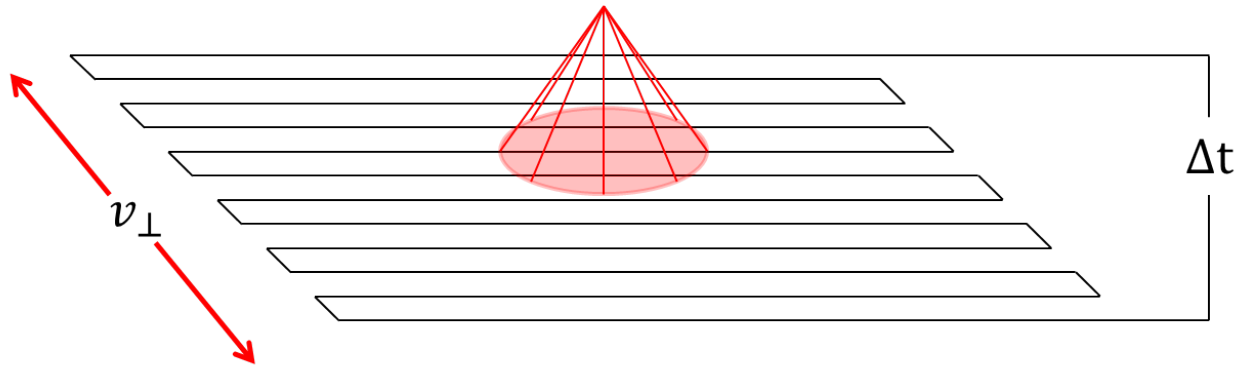

Figure 3.9: delay line readout in a single dimension. The induced signals on the wire from the charge cloud propagate at an effective speed of $v_\perp$ towards either end. Position of the ion hit is proportional to the time difference between the signals.

To read the signals from the MCP and the delay lines, a set of front-end electronics and data acquistion hardware was purchased from RoentDek. Starting from the detector, the first component is the FT12TP Feedthrough Flange with Signal Decoupler. While also providing the bias connections for the MCP and delay line anode, the FT12TP decouples the differential delay line signals from the signal and reference delay lines into single-line

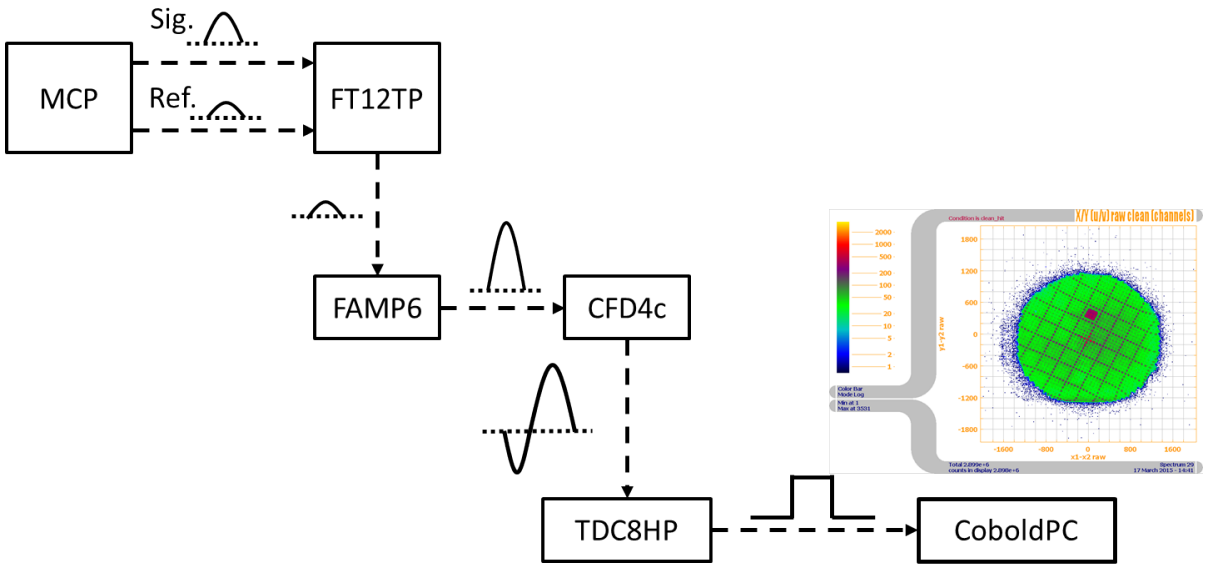

Figure 3.10: The signal processing and data acquisition process for the position-sensitive MCP for a single delay line pair. Between each module is a representation of the signal at that point in time.

signals via RC decoupling and transformer circuits. From there, the four delay line signals and the MCP contact signal are amplified by the FAMP6 Amplifier module to provide pulses of suitable height for discrimination and digitization.

Post-amplification, all five signals are routed to a CFD4c constant fraction discriminator. The constant fraction discriminator converts the unipolar signals from the amplifier into bipolar signals where the timing of the signal is independent of the signal height. The timing on each bipolar signal is then converted into a digital signal by the TDC8HP time-to-digital converter. The digitized timing signals for the delay lines can then be read by the data acquisition program, CoboldPC. For each MCP hit, CoboldPC writes to file the timing of all four delay line signals relative to the time of the MCP hit along with the ToF of the ion and a timestamp of when the hit occurred during the measurement. Fig. 3.10 is a block diagram illustrating the process for the signal and reference delay lines on one end of a delay line pair.

A conversion factor is required in order to compare the recorded position of an ion hit to the

physical position on the detector. The conversion factor for each dimension was determined through a calibration run with a pinhole mask provided by RoentDek. The mask is a 0.05 mm thick circular CuBe sheet with grid of holes spaced 1 mm apart center to center over its surface. A small window of nine squares located off-center indicates the rotational orientation of the mask.

With the mask mounted to the front ceramic ring of the detector, the detector was exposed to an alpha source for an extended period of time as seen in fig. 3.11. The recorded peak-to-peak distance in both dimensions was then compared to the 1 mm distance between the openings in the mask. The visible distortions where the gridlines appear to bend away from the center near the edge of the detector image in fig. 3.11 are due to the isotropic emission of the alpha particles from the source projected onto the flat mask.

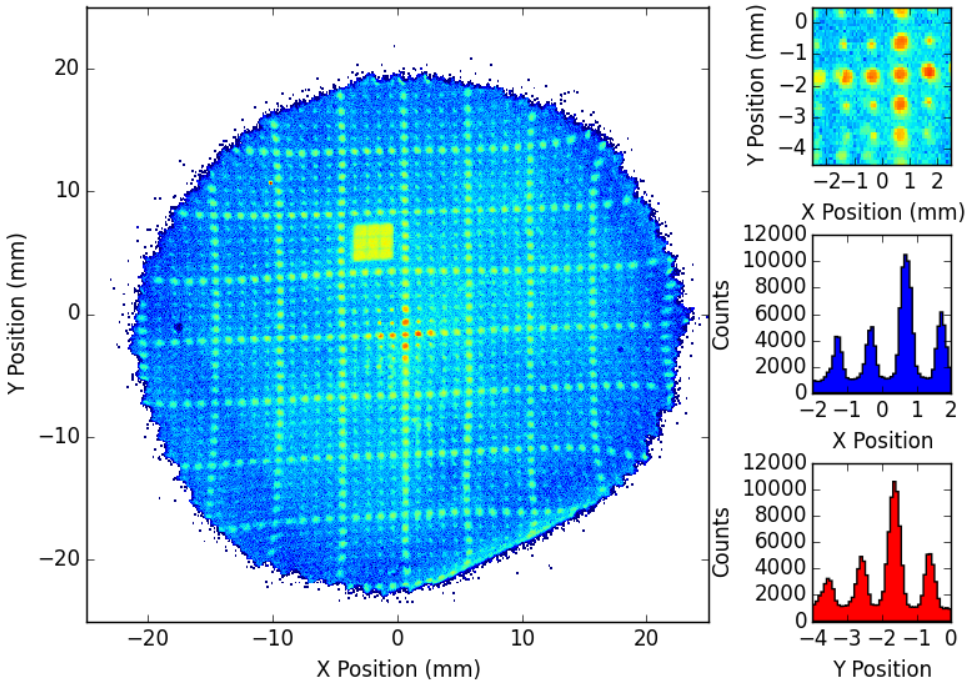

Figure 3.11: The main image is the face of the detector illuminated by an alpha source with the calibration mask installed. From top to bottom on the right is a zoomed in view of the center region and the projections of the counts in the zoomed-in region in the X and Y dimensions respectively.

3.3 Mass Measurement Procedure

The method of using the bunched beam from CARIBU to carry out a measurement is described here. For both ToF-ICR and PI-ICR methods, the process is identical except for the required excitations in the Penning trap and the subsequent analysis of the data. A diagram of the timing system can be seen in fig. 3.12.

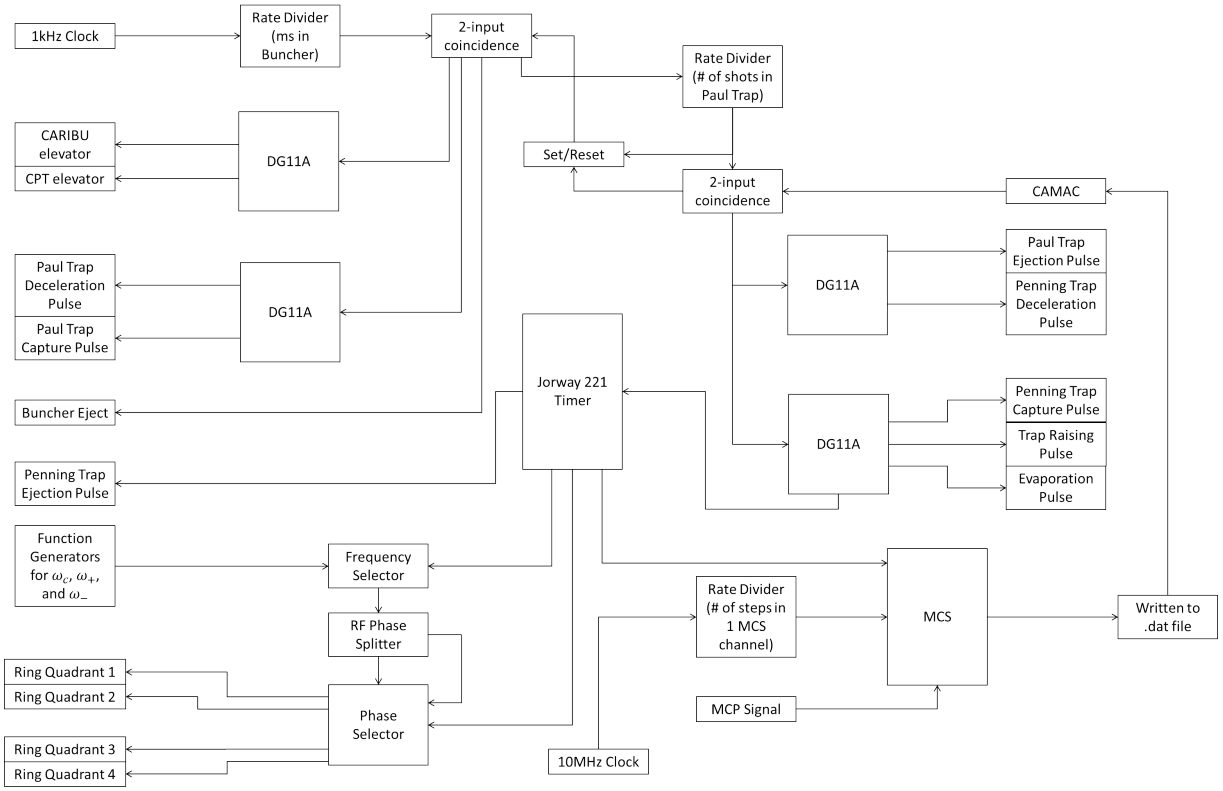

Figure 3.12: The timing pulses during a measurement cycle to transport ions from CARIBU to the CPT and excite them in the Penning trap.

The measurement cycle begins with a pulse from the 1 kHz clock. The signal from the clock triggers a rate divider module that will send an output signal after a user-defined number of counts has been reached. The number of counts required for the rate divider to send an output is the time in milliseconds that ions accumulate in the CARIBU buncher. The rate divider is typically set at 100 ms.

The output signal from the rate divider triggers a two-input coincidence module. The second trigger for the coincidence module is the output from the flip-flop module named Set/Reset that is sent when the Paul trap is empty. With the coincidence module triggered, four output signals are sent. Of the four, two go to DG11A precision delay generators, one goes to the CARIBU buncher to trigger an ejection, and one goes to a second rate divider.

The first DG11A is responsible for the CARIBU and CPT elevators. The CARIBU elevator is triggered on the order of 10 μs after the buncher eject pulse is sent, the exact value is dependent on the mass-to-charge ratio of the beam. The CPT elevator is similar in function to the CARIBU elevator, the ions with an energy of approximately 2 keV/e are brought down to ground potential in order to allow the ions to be captured by the Paul and Penning traps. Approximately 100 μs after the buncher eject pulse is sent, the CPT elevator is lowered from ground to a negative potential with the value dependent again on the mass-to-charge ratio of the beam.

The second DG11A is responsible for the deceleration and capture pulses of the Paul trap. These signals are sent approximately 10 μs after the CPT elevator is triggered and provide a DC gradient to capture ions. The deceleration pulse lowers the decel electrode on the Paul trap from 19.7 V to 7.7 V for 5 μs and the capture pulse lowers the S1 electrode from 6.2 V to -5.8 V for 13-15 μs. With the pulses complete, the Paul trap is returned to a harmonic potential.

The second rate divider is set by the user to dictate the number of bunches to be collected in the Paul trap. When the set number of bunches is reached, the output signal from the rate divider will be sent to the Set/Rest flip-flop module indicating that the Paul trap is full and to another two-input coincidence module. The second input to the coincidence module is a signal stating that the Penning trap is empty. This serves to ensure that nothing is present in the Penning trap when the Paul trap is ejected.

The output signal from the second two-coincidence module triggers the flip-flop module to indicate the Paul trap is ready to eject as well as triggering a second set of DG11A delay generators. In this set of delay generators, the first is responsible for the Paul trap ejection and Penning trap deceleration pulses and the second is responsible for the Penning trap capture, trap raising, and evaporation pulses.

The Paul trap ejects 30 ms after the final ion bunch was captured. The 30ms delay gives the final captured bunch time to cool through interactions with the He buffer gas. In the ejection, the S1 electrode is increased to 31.2 V while S3 and the top endcap electrodes are lowered to -48.8 V and -35.5 V respectively. The Penning trap deceleration pulse occurs simultaneously with the Paul trap ejection as the Penning trap deceleration electrode drops from 4.1 V to -146.1 V.

Approximately 50 μs after the triggering of the deceleration pulse, the Penning capture pulse occurs with the bottom endcap and correction tube electrodes dropped for roughly 10 μs and returned to their orginal settings over 1 μs. The voltages for the Penning trap throughout the capture, trap, and eject cycle are listed in table 3.2.

After the conclusion of the capture pulse, the trap raising pulse and evaporation pulse can be used to remove high energy ions from the trap. The trap raising pulse raises the ring electrode from -13.45 V to -5.9 V over about 2 ms while the evaporation pulse drops the top correction tube potential for 0.5 ms. For the PI-ICR measurements in this work, the evaporation and trap raising pulses were not used as they were observed to disturb the positions of the ions in the Penning trap.

At the conclusion of the trap raising and evaporation pulses, the ions have been transferred from the Paul trap to the Penning trap with the high energy ions removed.

Some 7 ms after the final capture in the Paul trap, the delay generator responsible for the Penning trap capture, trap raising, and evaporation pulses triggers a Jorway 221 delay

generator. The Jorway sets the delays for the remaining Penning trap pulses, namely the eigenmotion excitations and the Penning trap ejection pulse. Three triggers from the Jorway are sent to the Frequency Selector module that defines the duration windows of the ω_-, ω_+, and ω_c excitations. These windows are linked to a function generator for each frequency. Since the eigenmotion excitation process of the measurement cycle differs between the ToF-ICR and PI-ICR methods, the fine details of each will be discussed in sections 3.3.1 and 3.3.3.

The output from the Frequency Selector module is routed to the RF Phase Splitter module in order to copy the pulse and shift it 180° out of phase. The two pulses then enter the Phase Selector that dictates, based on user-set triggers from the Jorway, which pulse is applied to which quadrant of the Penning trap ring electrode. For a dipole excitation, the quadrants are divided into two adjacent pairs with each pair receiving a signal of opposite phase. For a quadrupole excitation, the quadrants that are opposite diagonally receive the same phase.

After the final excitation pulse has finished, the Jorway triggers the Penning trap ejection pulse and the potentials of the top endcap and correction electrodes are lowered for approximately 2 ms and then returned to their nominal values.

With the ions ejected from the trap, the Jorway triggers the LeCroy 3521a multi-channel scaler (MCS) to begin counting. The MCS possesses 256 channels that can be divided into time steps by an external input. The time step size per channel of the MCS is set by a rate divider used in concert with a 10 MHz clock. The typical time step used is 1 μs per channel. As the MCS is cycling through the channels, it reads the signal pulses from the MCP and records to file what channel it was in when an ion hit occurred. After the MCS has scanned through all 256 channels, a signal is sent back to the second two-input coincidence module to tell the timing system that the Penning trap is empty and the cycle can begin again.

The MCS is not actively used to record data for PI-ICR measurements, but it is still required to be running for the measurement cycle as it is responsible for the 'Penning trap empty signal'.

3.3.1 Time-of-Flight Method

For a ToF-ICR measurement, the first eigenmotion excitation in the Penning trap is a dipole excitation at the ω_+ frequency of any undesired ions. The dipole excitation will cause an increase in their orbital radius without disturbing the ions of interest (recall eq. 2.34). Once the orbit is larger than the aperture in the endcap, the ion will collide with the endcap on ejection and will not be detected. The applied duration of the ω_+ excitation is dependent on the difference in the ω_+ frequency of the contaminants and the desired ions. Smaller differences in the frequencies will require longer excitation times and lower amplitudes to avoid disturbing the ions of interest. If an appropriate combination of excitation time and amplitude is not chosen, the ions of interest are excited and the result is a lower time of flight and a possible shift in the measured resonant ω_c. This introduces a balancing act between keeping the excitation as short as possible while still cleaning sufficiently in order to minimize losses to radioactive decay and allow more time to be spent on the ω_c excitation. The ω_+ excitation typically has a duration of 50-400 ms. The function generator providing the pulse for the ω_+ excitation is a WW1071 Tabor waveform generator.

The second excitation is the ω_- dipole excitation lasting 10 ms. Following the cleaning, the remaining ions should still be at the center of the trap. The ω_- excitation establishes an initial magnetron orbit in the trap in preparation for the ω_c quadrupole excitation. The amplitude of the excitation is set to maximize the radius of magnetron orbit while still ensuring that the majority of ions will be ejected from the trap after the ω_c excitation. The function generator for the ω_- excitation is a Stanford Research Systems 30 MHz function generator.

The final excitation is the ω_c quadrupolar excitation. From eq. 2.41, if the applied frequency is equal to the cyclotron frequency of the ion then the initial magnetron motion set by the ω_- excitation is converted into reduced cyclotron motion as in fig. 2.5. After a full conversion, the ions in the trap have gained the maximum possible gain in orbital energy and will have the shortest ToF to the MCP upon ejection. If the frequency is not at ω_c, then the conversion is not fully completed and a longer ToF will result. Due to the relationship in eq. 2.46 it is desirable to excite the motion for as a long as possible in order to obtain higher precision, but the limiting factor is often the radioactive lifetime of the species under examination. Typically durations in the range of 50-2000 ms are used. The function generator for the ω_c excitation is a Stanford Research Systems 30MHz function generator.

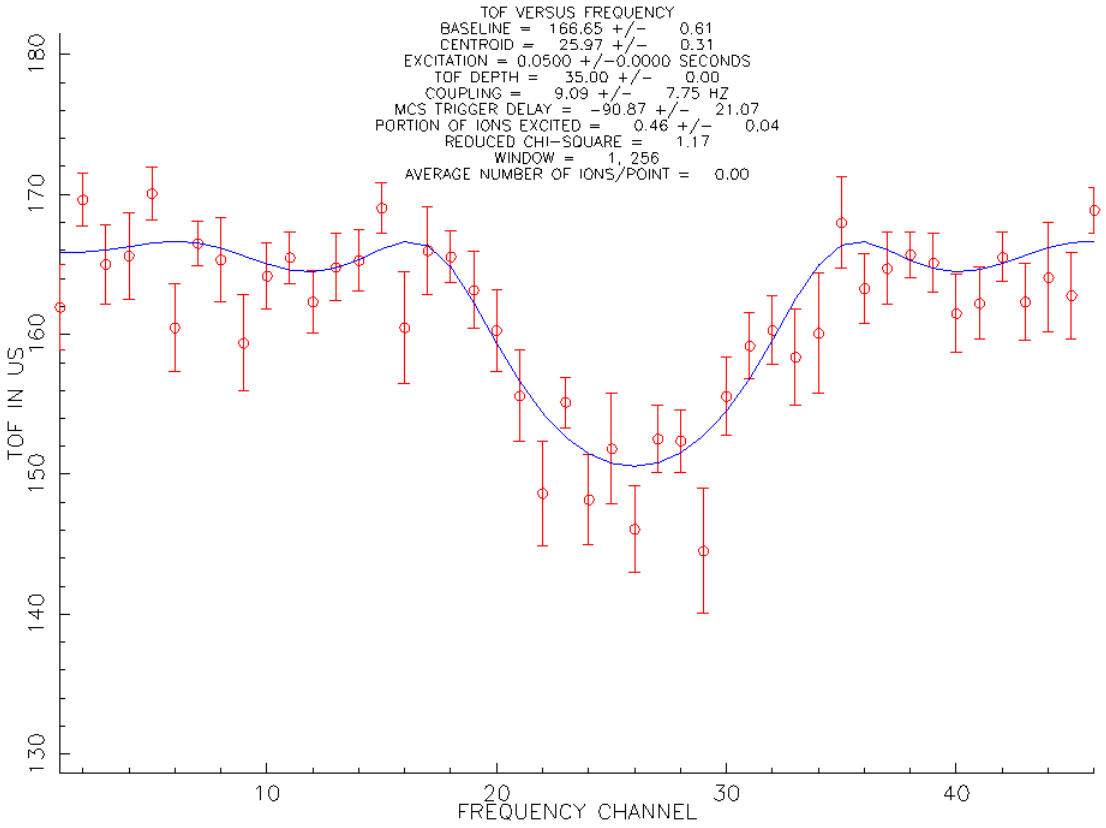

Figure 3.13: A sample ToF-ICR spectrum produced at the CPT.

The excitations are all applied sequentially with a delay of approximately 1 ms between them.

For each iteration of the measurement cycle, the excitations are repeated using a different ω_c frequency during the quadrupole excitation. With each new ω_c excitation over the user-defined range, the MCS stores the detector signals in a different column making the datafile a table of 256 rows and N columns where N is the number of the excitation frequencies. The average ToF is then plotted as a function of the applied quadrupole frequency with the ToF minimum corresponding to the resonant cyclotron frequency of the species under examination. A sample ToF spectrum is presented in fig. 3.13.

3.3.2 ToF-ICR Spectrum Fitting and Precision

The ToF of an ion that was ejected from a Penning trap and traveling through magnetic and electric field gradients is

$$t(\omega) = \int_{z_0}^{z} \sqrt{\frac{m}{2(E_0 - qV(z) - \mu(\omega)B(z))}} dz \tag{3.2}$$

with E_0 the initial axial energy, $V(z)$ the electrostatic potential along the axis, $\mu(\omega)$ the magnetic moment of the ion, and $B(z)$ the axial magnetic field along the path of travel. This equation, while accurate, is not adaptable for data analysis as $V(z)$ and $B(z)$ are varying functions and $\mu(\omega)$ depends on the orbital frequency in the trap which is dependent on the excitation parameters by extension. However, these factors should be taken into account for a function to fit the ToF spectrum.

In a paper by George *et. al.* [42], the energy produced by a square envelope excitation is stated as

$$E_r = \frac{4g^2 e^{-2\gamma t_{rf}}}{\sqrt{(4g^2 + \delta^2 - \tilde{\gamma}_1^2)^2 + 4\tilde{\gamma}_1^2\delta^2}} \left[\sin^2\left(\frac{\tilde{\omega_R} t_{rf}}{2}\right) + \sinh^2\left(\frac{\tilde{\gamma_R} t_{rf}}{2}\right)\right], \tag{3.3}$$

with δ the difference between the applied frequency ω_{rf} and the ω_c of the trapped ions, γ a

damping coefficient, t_{rf} the duration of the excitation, and g is an rf amplitude dependent coupling of the excitation to the ion motion. The remaining terms are the substitutions from the paper:

$$\tilde{\gamma}_1 \approx 2\gamma \frac{\omega_c}{\sqrt{\omega_c^2 + \omega_z^2}}, \tag{3.4a}$$

$$\tilde{\omega_R} = \frac{1}{\sqrt{2}} \sqrt{\sqrt{(\omega_R^2 - \tilde{\gamma}_1^2)^2 + 4\tilde{\gamma}_1^2\delta^2} + \omega_R^2 - \tilde{\gamma}_1^2}, \tag{3.4b}$$

$$\tilde{\gamma_R} = \frac{1}{\sqrt{2}} \sqrt{\sqrt{(\omega_R^2 - \tilde{\gamma}_1^2)^2 + 4\tilde{\gamma}_1^2\delta^2} - \omega_R^2 + \tilde{\gamma}_1^2}, \tag{3.4c}$$

and

$$\omega_R = \sqrt{4g^2 + \delta^2}. \tag{3.4d}$$

With $\omega_c \gg \omega_z$, eq. 3.4a can be written as $\tilde{\gamma}_1 \approx 2\gamma$. δ and g are angular quantities and can be awkward to use in comparison to the excitation parameters in seconds and Hertz, so the substitutions $g = \pi h/2$ and $\delta = 2\pi(\nu_i - \nu_c)$ are made. Inserting these substitutions into eq. 3.3 gives the radial energy of the ion in the trap to be

$$\begin{aligned} E_r(\gamma, t_{rf}, h, \nu_i, \nu_c) = {} & \frac{e^{-2\gamma t_{rf}} \pi^2 h^2}{\sqrt{(\pi^2 h^2 + 4\pi^2(\nu_i - \nu_c)^2 - 4\gamma^2)^2 + 64\gamma^2\pi^2(\nu_i - \nu_c)^2}} \\ & \times \left[\sin^2 \left(\frac{t_{rf}}{2\sqrt{2}} \sqrt{\sqrt{(\pi^2 h^2 + 4\pi^2(\nu_i - \nu_c)^2 - 4\gamma^2)^2 + 64\gamma^2\pi^2(\nu_i - \nu_c)^2} + \pi^2 h^2 + 4\pi^2(\nu_i - \nu_c)^2 - 4\gamma^2} \right) \right. \\ & \left. + \sinh^2 \left(\frac{t_{rf}}{2\sqrt{2}} \sqrt{\sqrt{(\pi^2 h^2 + 4\pi^2(\nu_i - \nu_c)^2 - 4\gamma^2)^2 + 64\gamma^2\pi^2(\nu_i - \nu_c)^2} - \pi^2 h^2 - 4\pi^2(\nu_i - \nu_c)^2 + 4\gamma^2} \right) \right] \end{aligned} \tag{3.5}$$

When the excitation is resonant and $\nu_i = \nu_c$, eq. 3.5 reduces to

$$E_{r,0}(\gamma, t_{rf}, h) = \frac{e^{-2\gamma t_{rf}} \pi^2 h^2}{\pi^2 h^2 - 4\gamma^2} \sin^2 \left(\frac{t_{rf}}{2} \sqrt{\pi^2 h^2 - 4\gamma^2} \right). \tag{3.6}$$

With an expression for the radial energy the trapped ions gain through excitation, a model is now used instead of eq. 3.2. If the velocity of the ions from the trap to the detector is

constant, then their kinetic energy can be written as $T = T_b + T_r$ where T_b is the baseline energy that the ions would possess if no excitation was applied and T_r the radial energy given to the ions during the excitation. From there, the time of flight is derived to be

$$t_{tof} = \frac{b}{\sqrt{1 + \frac{T_r}{T_{r,0}}\left[\left(\frac{b}{b-d}\right)^2 - 1\right]}}, \tag{3.7}$$

where b is the baseline ToF when no excitations are applied, d is the depth of the on-resonance ToF minima, and $T_{r,0}$ the radial energy when the ToF is a minimum. This derivation was first done by former CPT students Jon Van Schelt and Shane Caldwell and can be seen in [43].

While eq. 3.7 gives the true ToF, there is a noticeable delay between the ejection of ions from the Penning trap and when the MCS begins recording. The addition of the parameter s is used to account for that time delay. The true baseline and ToF can then be written in terms of the recorded values, b' and t'_{tof}, and s:

$$t'_{tof} = \frac{b' + s}{\sqrt{1 + \frac{T_r}{T_{r,0}}\left[\left(\frac{b'+s}{b'+s-d}\right)^2 - 1\right]}} - s. \tag{3.8}$$

In the ideal scenario of having only one species in the trap, eq. 3.8 is all that is required. However, the possible presence of contaminants present in the trap, despite the application of ω_+ cleaning, must be taken into account and one further modification must be made. The ions of interest are resonantly excited and the shape of their ToF spectrum will be similar to that from the calibrant spectrum. The contaminant species will in general be off resonance and have a different shape. The recorded ToF spectrum is the weighted average of both components. Well off resonance, the baseline remains unchanged for both species. Therefore a second parameter n is introduced representing the relative fraction of ions of the desired

species in the trap and the fitting function becomes a weighted sum of the full-depth ToF function and a flat baseline:

$$t'_{tof} = (b' + s)\left(1 - n + \frac{n}{\sqrt{1 + \frac{T_r}{T_{r,0}}\left[\left(\frac{b'+s}{b'+s-d}\right)^2 - 1\right]}}\right) - s. \tag{3.9}$$

The precision of a ToF-ICR measurement has the greatest dependence on the excitation time t_{rf} and the total number of ions detected N_i. Through extensive data collection at ISOLTRAP, it has been found that the statistical uncertainty of an ω_c measurement is [44]

$$\frac{\delta m}{m} = \frac{\delta\omega_c}{\omega_c} \approx \frac{1}{R\sqrt{N_i}} = \frac{m}{qB}\frac{1}{t_{rf}\sqrt{N_i}}, \tag{3.10}$$

where R is the resolving power $\omega_c/\Delta\omega_c$.

Since the magnetic field of the CPT is fixed at approximately 5.7 T and ions produced by CARIBU only have +1 or +2 charge states, maximizing the duration of the ω_c excitation and repeating the measurement to amass a greater number of detected ions are the only options to increase the precision. However, when measurements of short-lived nuclei are carried out, the excitation time becomes limited by the half-lives of the species being examined and collecting more statistics is the only viable way of increasing precision. As these short-lived nuclei are generally produced much more weakly from CARIBU, measurements on the timescale of hours are required to achieve the desired statistical uncertainty.

3.3.3 Phase-Imaging Method

For the phase-imaging measurements at the CPT, the chosen scheme was the direct measurement of ω_c described in section 2.5 with an extra delay to compensate for the millisecond level response time of the mechanical relays in the Frequency Selector module. The function

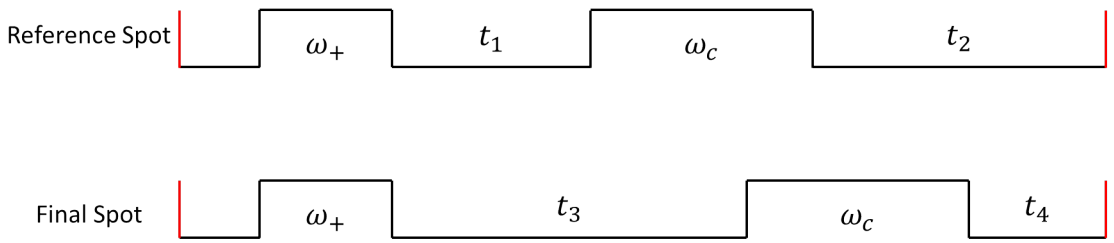

Figure 3.14: The excitation scheme for a direct PI-ICR measurement of the cyclotron frequency used at the CPT. The red lines indicate the injection and ejection of ions into and out of the Penning trap.

generator used for the eigenmotion excitations in phase-imaging measurements at the CPT was the Tabor waveform generator used for the ω_+ dipole excitations described in section 3.3.1.

To filter out background noise, two conditions are set in the CoboldPC acquisition program and both must be met for the data to be recorded. The first condition is that all four delay line signals from an MCP hit must register within a 50 ns window following the hit, ensuring that signals from the delay lines correspond to a ion hit on the MCP. The second condition is that the MCP hit must occur within a set ToF window relative to the ejection pulse. From the voltage settings of the ToF electrodes, we can estimate when the ions from the Penning trap should hit following the ejection and only accept counts within that window. Currently the ToF window is set to allow counts that have a ToF between 85 μs to 100 μs.

The measurement process for PI-ICR is always divided into three steps: production of the center image, production of the reference image, and production of the final image. To produce the center image, the ions are simply held in the Penning trap for a duration typically on the order of ms with no excitations applied prior to ejection.

For the reference phase image, the captured ions undergo a dipolar ω_+ excitation for 3-5 ms. Now traveling in an orbit with a frequency of ω_+, the ions are allowed to accumulate phase for a time t_1. After the phase accumulation time has elapsed, a quadrupolar excitation at ω_c

is applied for 0.6 ms to convert the ion motion from reduced cyclotron motion to magnetron motion. Following the quadrupolar excitation there is a second delay of t_2 where the ions accumulate another phase while undergoing magnetron motion. After the second delay has elapsed, the ions are ejected. Fig. 3.14 provides a visual example of the modified excitation scheme.

For the final image, there is a delay of time t_3 between the dipolar ω_+ excitation and quadrupolar ω_c excitation where the ions are accumulating a phase while undergoing reduced cyclotron motion. After the conversion to magnetron motion, there is a delay of time t_4 prior to ejection to allow the accumulation of phase via magnetron motion.

If the delays are fixed such that the difference between delays while accumulating a phase under reduced cyclotron motion $(t_3 - t_1)$ and while accumulating a phase under magnetron motion $(t_2 - t_4)$ are equal, the differences are then equivalent to a single phase accumulation time t as discussed in section 2.5. A derivation of this relation is shown in the appendix A.1.

One final mechanical detail of the PI-ICR measurement method at the CPT concerns the presence of contaminants. With the excitation scheme for a PI-ICR measurement at the CPT, it was not possible to remove contaminants through ω_+ excitations for technical reasons.

3.3.4 PI-ICR Spectrum Fitting and Precision

In comparison to the fitting function for ToF-ICR measurements, the analysis behind the PI-ICR analysis is rather straightforward. As mentioned in section 3.2.3, the data acquisition program CoboldPC records the timing of the four delay line signals relative to the MCP hit along with a timestamp of when the hit occurred during the measurement. The position of an ion hit in one dimension is then determined by the time difference between the two

delay line signals in that respective dimension multiplied by the dimensional conversion factor determined through the detector calibration. The one-dimensional position data for a measurement is plotted as a histogram, see fig. 3.15, which is then fit to a Gaussian (eq. 3.11) via a non-linear least-squares minimization:

$$y = A \exp\left(\frac{-(x-b)^2}{2c^2}\right) + d. \tag{3.11}$$

The mean of the Gaussian, b in eq. 3.11, is then taken to be the center position of the image in that dimension. In order to maintain as clean a spectrum as possible, each of the three images are recorded in a separate data file.

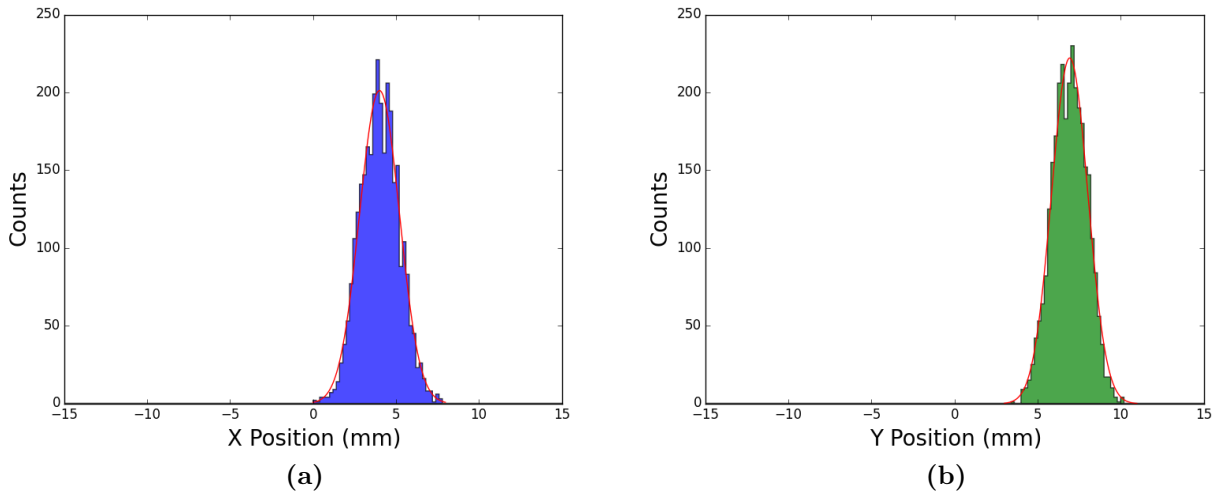

Figure 3.15: Position histograms of an image in the X (a) and Y (b) dimensions.

With the positions of the three images now determined and N calculated from a ToF-ICR measurement, the angle ϕ and the frequency ω_c can be calculated. Because the phase accumulates in the direction of the ion's orbit, it is convenient to modify eq. 2.47 slightly. An ion in the trap that undergoes reduced cyclotron motion orbits in a counter-clockwise direction, whereas an ion undergoing magnetron motion orbits in a clockwise direction. The result is that in a direct cyclotron frequency measurement, the overall phase accumulation

is in the counter-clockwise direction. Using eq. 3.12 ensures that the correct angle between the reference and final images is used in the frequency calculation:

$$\omega_c = \frac{\phi + 2\pi N}{t}, \quad \text{where } \phi = \text{atan2}\left(Y_f, X_f\right) - \text{atan2}\left(Y_i, X_i\right). \tag{3.12}$$

Otherwise a visual inspection of the reference and final images would be required to determine whether the angle should be ϕ or $2\pi - \phi$.

The precision of a PI-ICR follows the same form as for ToF-ICR measurements, eq. 3.10, with the precision equal to the inverse of the resolving power and statistical uncertainty [30]:

$$\frac{\delta m}{m} = \frac{\delta \omega_c}{\omega_c} \approx \frac{1}{R\sqrt{N_i}} = \frac{m}{qB}\frac{2\Delta r}{tr\sqrt{N_i}}. \tag{3.13}$$

Again, like the precision for ToF-ICR, the precision of PI-ICR is dictated by the time the ions spend in the trap and the statistics gathered in the measurement. While the radius of the ion orbit in the trap and the radial image spread Δr contribute to the overall precision, the radius of the orbit cannot exceed the radius of the aperture in the Penning trap and the radial spread will not vary significantly in a properly tuned system. Since the timescale of the accumulation time is typically an order of magnitude less than the ToF-ICR excitation time to obtain the same level of precision, it becomes less of a limiting factor for measurements of short-lived nuclei. This point will be discussed further in section 4.

4 Data Analysis and Results

'A proof is a proof. What kind of proof?
It's a proof. A proof is a proof
and when you have a good proof,
it's because it's proven.'
-Jean Chrétien

The results of five mass measurements of short-lived species from CARIBU to demonstrate the proof-of-principle for PI-ICR measurements will be presented. A comparison of the relative merits of the ToF-ICR and PI-ICR methods will conclude this chapter.

4.1 Systematic Effects and Instrumental Contributions

The experimental apparatus and the data analysis were carefully examined in order to discern any systematic or instrumental contributions to the uncertainty in a frequency measurement. The drift of the magnetic field and the interaction between multiple species in the trap were identified as possible sources of instrumental and systematic uncertainties.

4.1.1 Magnetic Field Drift

The mass of a species under examination is determined by the ratio of the masses of a reference ion and the ion under study through measurements of their respective cyclotron frequencies. Since the reference frequency and the frequency of each unknown species are measured at different times, it is vital that the magnetic field remain stable over the period that the measurements are carried out. To verify the stability of the magnetic field, measurements of the resonant cyclotron frequency of ^{133}Cs ions provided by the SIS are examined

over time for shifts in frequency.

In fig. 4.1, ^{133}Cs cyclotron frequency measurements via the ToF-ICR technique are plotted over a period of eight months from January to August of 2015 with a weighted linear fit applied through a least squares regression. Over this time any possible shifts in cyclotron frequency due to the magnetic field were found to be less than -0.4 mHz per day, corresponding to a magnetic field shift of -6×10^{-10} T per day. As the long-term drift is less than 1ppb per day, the magnetic field drift will not have a noticeable effect on the measurements in this work. The measurements used for fig. 4.1 are listed in table 4.1.

Date	Frequency (Hz)	Excitation Time (ms)
January 6th	657 844.426(23)	100
January 22nd	657 844.5153(72)	500
February 4th	657 844.338(53)	100
February 4th	657 844.530(41)	100
February 4th	657 844.479(10)	500
February 4th[a]	657 844.477(16)	-
February 5th	657 844.453(59)	100
February 9th	657 844.492(72)	100
February 9th	657 844.591(16)	500
February 9th	657 844.528(18)	500
February 9th[a]	657 844.562(52)	-
May 13th	657 844.39(14)	100
May 13th	657 844.42(16)	100
May 13th[a]	657 844.40(11)	-
June 19th	657 844.385(36)	300
June 30th	657 844.458(20)	200
August 7th	657 844.556(36)	100
August 7th	657 844.461(22)	200
August 7th[a]	657 844.486(36)	-

[a] Weighted mean of measurements taken on the same day.

Table 4.1: ToF-ICR cyclotron frequency measurements of $^{133}Cs^{+}$ used in fig. 4.1. For data taken on the same day, a weighted average was used.

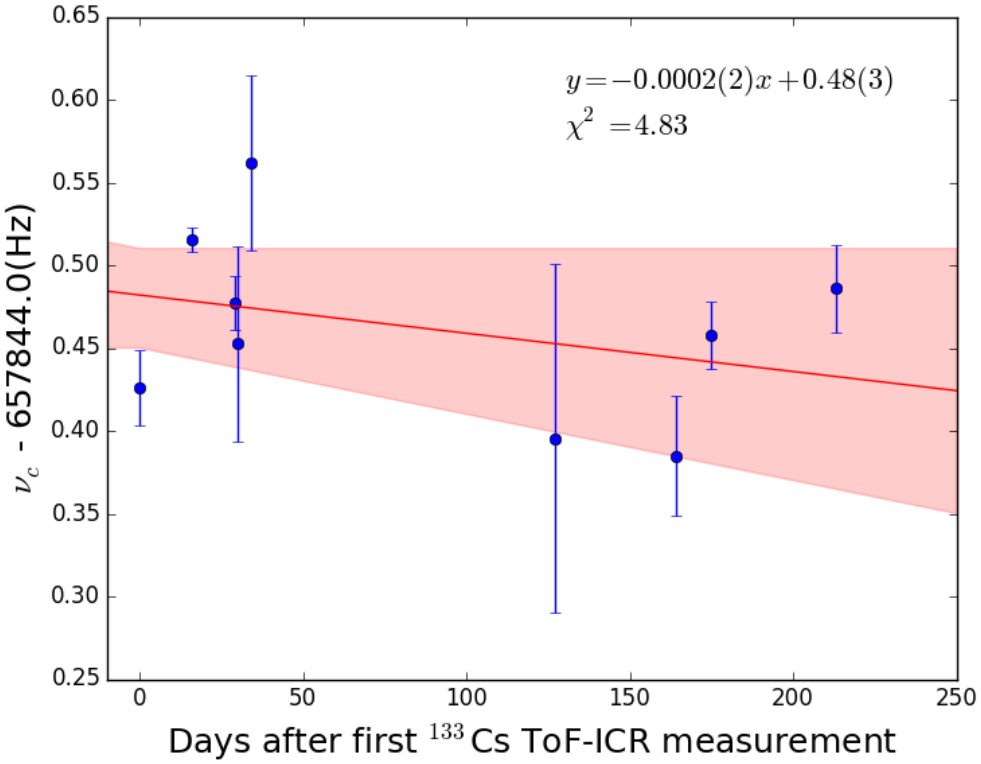

Figure 4.1: $^{133}Cs^{+}$ cyclotron frequency measurements over an eight-month period. The weighted linear fit applied to the measurements is indicated by the red line.

4.1.2 Multiple Species in the Trap

Since the SIS is a surface ionization source, it is manufactured to produce a single species. While contaminant alkali ions may be present in the anode of the SIS, the duration of the pulses to transport the ions to the trap are set for the charge-to-mass ratio of ^{133}Cs ions. As a result ^{133}Cs is the only species observed in the trap when it is in use.

The same cannot always be said for CARIBU. It is common for contaminants such as isobars of the species under examination or hydrocarbons to find their way to the trap. In this work, contaminants were observed at masses $A = 142$ and $A = 143$, whereas for masses $A = 144$ and $A = 146$ only the species under examination were observed in the trap. As a visual example, fig. 4.2 displays the reference and final phase images for $A = 142$. Three distinct

species can be seen: ^{142}Cs, ^{142}Xe, and the CARIBU contaminant $^{127}ICH_3$. For comparison, the reference and final phase images for ^{133}Cs are displayed in fig. 4.3.

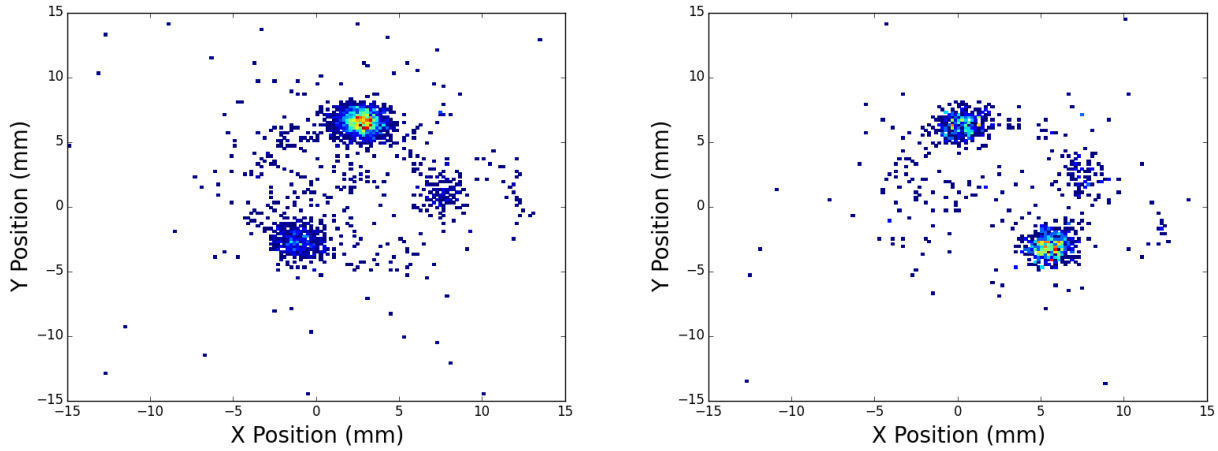

Figure 4.2: The reference (a) and final (b) phase images for proof-of-principle ^{142}Cs and ^{142}Xe measurements. The three spots in each image correspond to the three most abundant species in a CARIBU beam at $A = 142$. The most prominent is the contaminant $^{127}ICH_3$, followed by ^{142}Cs and ^{142}Xe.

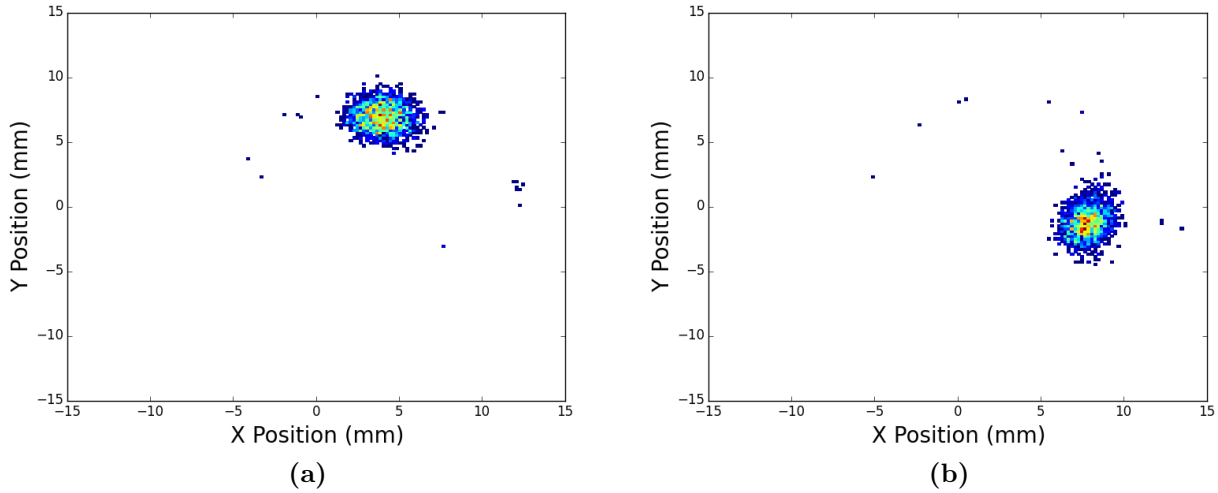

Figure 4.3: The reference (a) and final (b) phase images for a proof-of-principle ^{133}Cs measurement.

The effect due to the presence of the contaminant ions on the $A = 142$ and $A = 143$

measurements will be discussed on a case-by-case basis in section 4.2.3.

4.2 PI-ICR Results

4.2.1 ^{133}Cs Measurements

A total of twenty-one independent PI-ICR measurements for ^{133}Cs were taken over ten days in June of 2015. These measurements are sorted into four groups based upon the date they were taken. For each measurement group the weighted mean, internal, and external variances were calculated through eqs. 4.1a, 4.1b, and 4.1c respectively:

$$\bar{\nu} = \frac{\sum_i \nu_i \sigma_i^{-2}}{\sum_i \sigma_i^{-2}}, \tag{4.1a}$$

$$\sigma_{int}^2 = \frac{1}{\sum_i \sigma_i^{-2}}, \tag{4.1b}$$

and

$$\sigma_{ext}^2 = \frac{\sum_i \sigma_i^{-2}(\nu_i - \bar{\nu})^2}{\sum_i \sigma_i^{-2}(N-1)}. \tag{4.1c}$$

In all cases, the larger variance was taken as the uncertainty of the weighted mean. The independent measurements used to calculate the weighted means are listed in the appendix in table A.1.

These frequencies are then compared to two sets of ToF-ICR data with excitation times of 100 ms and 500 ms taken in January and February of 2015. The results of the ^{133}Cs measurements are summarized in table 4.2. With the PI-ICR measurements taken approximately 100 days after the ToF-ICR measurements, we would expect a systematic shift of 0.02 Hz based on

Date	Frequency (Hz)	Int. Unc.(Hz)	Ext. Unc.(Hz)	$\Delta\nu_{0.1s}$ (Hz)	$\Delta\nu_{0.5s}$ (Hz)
June 12th	657 844.4406	0.0030	0.036	0.000(43)	-0.074(39)
June 19th	657 844.4813	0.0059	0.082	-0.040(86)	-0.033(85)
June 22nd	657 844.4782	0.0053	0.051	0.037(56)	-0.036(53)
June 22nd	657 844.4345	0.0085	0.067	-0.006(71)	-0.079(69)

Table 4.2: Cyclotron frequencies of $^{133}Cs^{+}$ measured using the PI-ICR method. The 3^{rd} and 4^{th} columns contain the calculated internal and external uncertainties of the weighted mean. In the 5^{th} and 6^{th} columns are the differences between the PI-ICR value and the measured ToF-ICR values for 100 ms and 500 ms excitation times respectively. The measurements on June 22^{nd} were separated into two groups due to a change in the amplitude of the dipole excitation.

our analysis of the magnetic field drift in section 4.1.1.

The measurement of frequency as a standard to an expected value gives an indication to the presence of instrumental effects. In comparing the ^{133}Cs PI-ICR measurements with previous ToF-ICR measurements carried out at the CPT it is difficult to perceive a shift in this data due to either the magnetic field drift or any instrumental effect. The frequency measurements are consistent and there are no systematic effects associated with this new technique.

One final observation of these initial PI-ICR measurements concerns the uncertainties. In a direct comparison of the internal and external uncertainies of the weighted means, the internal uncertainty of the PI-ICR measurements appears to be underestimated by an approximate factor of 10.

The independent PI-ICR measurements for ^{133}Cs are plotted in fig. 4.4 along with their weighted mean. For most of the individual measurements, the estimated error bars are significantly less in comparison to the scatter in the data (the external uncertainty of the weighted mean). The larger of the two uncertainties was used in all cases.

4.2.2 Measurements with CARIBU Beams

A total of thirty-four independent PI-ICR measurements of species produced by CARIBU were taken at the CPT. With the exception of four measurements of ^{146}Cs taken on July 17th, all PI-ICR measurements were taken in a seven-day period in June of 2015.

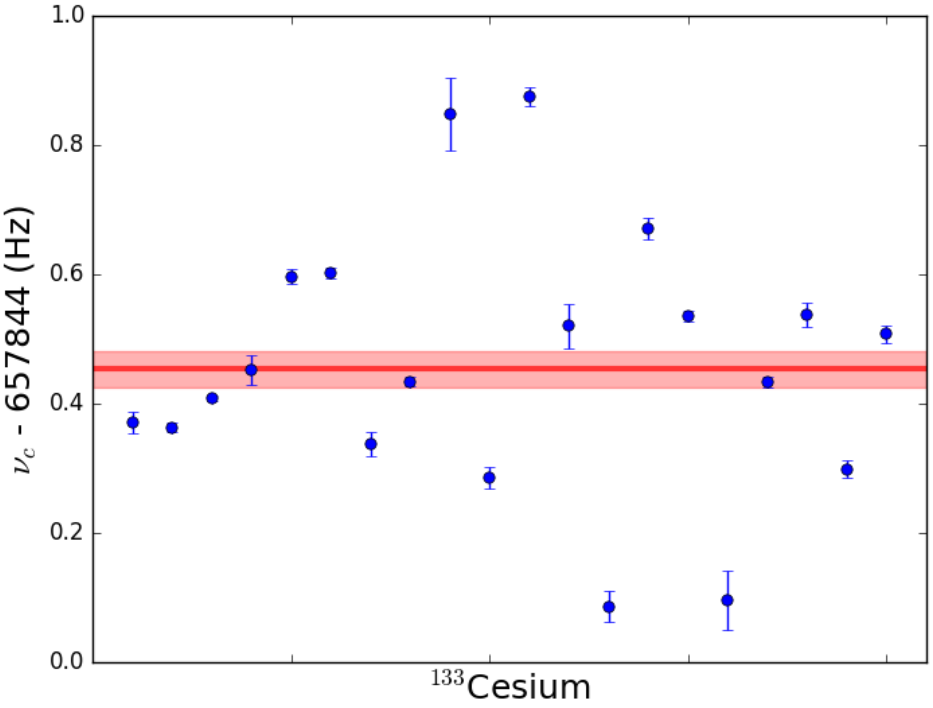

Figure 4.4: All independent PI-ICR measurements of all $^{133}Cs^{+}$ conducted in this work. The weighted mean is represented by the red line. The red shaded area depicts the uncertainty in the mean.

For each species under examination, the process was the same as for a set of ^{133}Cs measurements as described in section 4.2.1. The weighted means of the frequencies for the species under examination are listed in table 4.3. The independent measurements used to calculate the weighted means are listed in table A.2 located in the appendix section A.3.

To calculate the mass from the cyclotron frequency we return to the relationship stated in

Species	Frequency (Hz)	No. of Ind. Measurements	Int. Unc. (Hz)	Ext. Unc. (Hz)
$^{142}Cs^{+}$	616 040.4340	10	0.0042	0.036
$^{142}Xe^{+}$	616 015.8067	10	0.0053	0.052
$^{143}Cs^{+}$	611 717.0673	8	0.0039	0.037
$^{144}Cs^{+}$	607 446.9188	1	0.0082	0.109[a]
$^{146}Cs^{+}$	599 086.7054	5	0.0134	0.102

[a] With only one independent measurement, the external uncertainty for the $^{144}Cs^{+}$ frequency measurement could not be calculated. As a result, the listed external uncertainty for $^{144}Cs^{+}$ was determined by calculating the average ratio of external to internal uncertainties from the other PI-ICR measurements and multiplying the the $^{144}Cs^{+}$ internal uncertainty by that value.

Table 4.3: Weighted means of the cyclotron frequencies of the five nuclei measured using the PI-ICR method. The 4^{th} and 5^{th} columns are the calculated internal and external uncertainties.

section 2.2, eq. 2.14:

$$\omega_c = 2\pi\nu_c = \frac{qB}{m}. \tag{4.2}$$

The magnetic field is determined through a measurement of the cyclotron frequency associated with a well known-mass. Substituting the result of cyclotron frequency measurement, ν_b, of the well-known mass, m_b, into eq. 4.2 in place of the magnetic field gives the relation

$$m_a = \frac{q_a(m_b - q_b m_e)\nu_b}{q_b\nu_a} + q_a m_e, \tag{4.3}$$

where m_e is the mass of the electron.

The uncertainty of the unknown mass, m_a, is determined by adding the contributions of the components to the uncertainty in quadrature:

$$\delta_{m_a} = \sqrt{\left(\frac{q_a\nu_b}{q_b\nu_a}\right)^2\delta_{m_b}^2 + \left(\frac{q_a(m_b - q_b m_e)}{q_b\nu_a}\right)^2\delta_{\nu_b}^2 + \left(\frac{q_a(m_b - q_b m_e)\nu_b}{q_b\nu_a^2}\right)^2\delta_{\nu_a}^2 + \left(q_a - \frac{\nu_b}{\nu_a}\right)^2\delta_{m_e^2}}. \tag{4.4}$$

While the δ_{m_e} is negligible, it is included for the purpose of completeness. The calibrant species for these measurements was ^{133}Cs. The weighted mean of the PI-ICR measurements

in table A.1, 657844.454(27) Hz, was taken as the calibrant frequency.

The results of the mass measurements from CARIBU beams are summarized in table 4.4 in both atomic mass units (u) and mass excess (keV) with a comparison to the values published in the 2012 AME along with the frequency ratio to ^{133}Cs. The auxiliary data used to calculate the masses and mass excesses are listed in table 4.5.

Species	$\nu_{a^+}/\nu_{^{133}Cs^+}$	Atomic Mass (μu)	Mass excess (keV)	$\Delta m_{CPT-AME}$ (keV)
^{142}Cs	1.067 859 21(11)	141 924 274(15)	-70 538(14)	-20(16)
^{142}Xe	1.067 901 91(10)	141 929 948(13)	-65 252(12)	-23(13)
^{143}Cs	1.075 406 407(79)	142 927 333(10)	-67 688.6(9.7)	-15(24)
^{144}Cs	1.082 966 15(20)	143 932 060(26)	-63 285(25)	-14(35)
^{146}Cs	1.098 078 87(19)	145 940 615(26)	-55 317(24)	253(46)

Table 4.4: Frequency ratios for the measured species from CARIBU beams using the PI-ICR method. The masses, and by extension the mass excesses, are derived from the frequency ratios.

Constant	Value
^{133}Cs$^+$ Mass	132.904 903 3811(90)
m_e	548.579 909 46(22) μu
Mass energy conversion factor	931 494.061(21) keV/c^2/u

Table 4.5: Auxiliary data used in the calculation of results. All values taken from [14].

4.2.3 Discussion of the Results

The masses measured in this thesis were chosen because of their ease of production from CARIBU and the fact that they are well known, with the exception of ^{146}Cs, thus providing a solid comparison value for the proof-of-principle PI-ICR measurements. Of the five masses measured, ^{142}Cs, ^{142}Xe, and ^{146}Cs do not agree within 1σ with the 2012 AME value. In table 4.6, the most significant inputs contributing to the 2012 AME values are compared to the results in table 4.4.

Species	Experiment/Type of Measurement	Mass excess (keV)	$\Delta m_{CPT-previous}$ (keV)
^{142}Cs	CPT [7]	-70 511(10)	-27(17)
^{142}Xe	ISOLTRAP [45]	-65 229.7(2.7)	-23(13)
^{143}Cs	Q_{β^-} endpoint [46]	-67 709(38)	20(39)
^{144}Cs	Q_{β^-} endpoint [46] [47] [48]	-63 287(37)	2(44)
^{146}Cs	Q_{β^-} endpoint [46] [47] [48]	-55 590(60)	273(65)

Table 4.6: Mass results of previous experiments for the species examined in this thesis. In all cases, the value used was the most significant input value for that species in the 2012 AME.

^{142}Cs: ^{142}Cs has a half-life of 1684(14) ms [49] and a yield of 2.53 per 100 fissions from ^{252}Cf [35]. The most significant input value for the 2012 AME mass value was a ToF-ICR measurement carried out by the CPT in 2009 [7]. This measurement along with two other input values were the dominant inputs to the mass table. A subsequent CPT measurement in 2012 [8] agrees with the earlier CPT measurement. The PI-ICR value disagrees with the primary input and the adjusted mass from the 2012 AME as well as the subsequent CPT measurement by 1.6σ, 1.3σ, and 1.9σ respectively. While the discrepancies are not large, they are significant.

^{142}Xe: ^{142}Xe has a half-life of 1230(20) ms [49] and a yield of 0.368 per 100 fissions from ^{252}Cf [35]. The ISOLTRAP measurement of ^{142}Xe from 2009 [45] is a ToF-ICR measurement and the primary mass input for the mass evaluation. The PI-ICR measured value disagrees with this value by a factor of 1.8σ. As with ^{142}Cs, this is a small but significant discrepancy.

The discrepancies between the published values and the PI-ICR measurements of ^{142}Cs and ^{142}Xe are suspected to be due to the presence of multiple species in the trap at $A = 142$. As shown in fig. 4.2, the contaminant $^{127}ICH_3$ is the most prominent species in the trap with an average ion count per measurement of 1.4 times more intense than ^{142}Cs and 7.4 times more intense than ^{142}Xe. The atomic mass of $^{127}ICH_3$ was measured to be 141.927962(28) u, agreeing with the value calculated with data taken from the 2012 AME.

^{143}Cs: ^{143}Cs has a half-life of 1791(7) ms [50] and a yield of 0.743 per 100 fissions from ^{252}Cf [35]. A Q_β endpoint measurement from the Isotope Separator On Line Detector (ISOLDE) in 1991 [46] is the most recent of three Q_{β^-}-endpoint measurements that are averaged to calculate the adjusted value reported in the 2012 AME. The PI-ICR value agrees with this value and the adjusted mass value. As well, a ToF-ICR measurement by the CPT in 2012 [8] produced a result that agrees with the PI-ICR value. In comparison to the disagreement with the expected values at $A = 142$, the lack of a shift from the expected value for ^{143}Cs is likely due to ^{143}Cs being the more prevalent species in the trap with an average ion count per measurement of 3.4 times more than the contaminant.

^{144}Cs: ^{144}Cs has a half-life of 994(6) ms [51] and a yield of 0.549 per 100 fissions from ^{252}Cf [35]. The primary input value for ^{144}Cs in the 2012 AME is the average of three Q_{β^-} endpoint measurements from 1991 [46], 1987 [47], and 1981 [48]. The PI-ICR value agrees with this value, the adjusted mass value, and a CPT measurement in 2012 [8].

^{146}Cs: ^{146}Cs has a half-life of 321(2) ms [52] and a yield of 2.58E-2 per 100 fissions from ^{252}Cf [35]. Even though one of the PI-ICR measurements for ^{146}Cs was taken a month apart from the others, it was included in the analysis because of the long-term stability of the magnetic field. The PI-ICR measurement of ^{146}Cs disagrees with both the adjusted value in the mass evaluation and the primary input value, an average of three Q_{β^-} endpoint measurements [46] [47] [48], by 5.4σ and 4.2σ respectively. In comparison, a ToF-ICR measurement at the CPT in 2012 [8] agrees with the PI-ICR measurement. That separate measurements with the same spectrometer using two different measurement techniques produced results that agree speaks to the reliability of the ^{146}Cs PI-ICR measurement.

The two neutron separation energies that can be calculated from the Cesium masses determined in this work in comparison to the values in the 2012 AME are shown in fig. 4.5. The slopes of the curves for the calculated Cesium energies from N=91 to N=93 are more consistent with those of the Xenon and Barium energies, giving added confidence to our

^{146}Cs measurement.

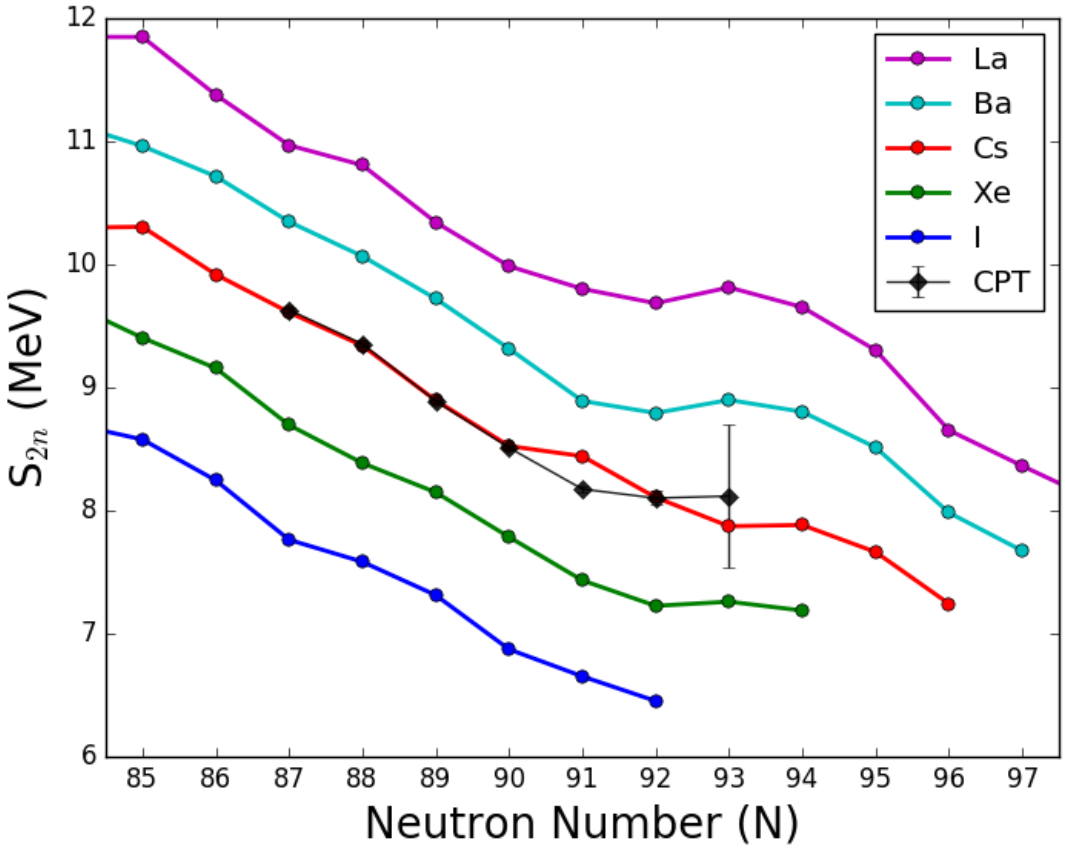

Figure 4.5: The two neutron separation energies for Iodine to Lanthanum from N=85 to 97. The coloured lines represent the separation energies from the 2012 AME. Superimposed in black over the Cesium line are the separation energies of the Cesium isotopes examined in this thesis. The error bars for the calculated separation energies are smaller than the markers with the sole exception being ^{148}Cs. Mass values from the 2012 AME were used in conjuction with the measured masses when required for the separation energy calculations.

In total, five atomic masses were measured in this work. Of the five, three were accurate. The two discrepent masses were of species under a heavy contaminant influence, illustrating the importance of ensuring that only one species is present in the trap during measurement.

4.3 Future Outlook of Mass Measurements at the CPT

The apparatus to carry out phase-imaging measurements at the CPT was installed and commissioned. With the new system commissioned, we can look forward to extending our program of mass measurements far from stability.

As we push out further from stability, we encounter nuclei with ever shorter lifetimes produced in decreasing fission yields from the ^{252}Cf source. In previous measurement campaigns of neutron-rich nuclei with ToF-ICR, fission fragment branches on the order of 10^{-4} have been reached with half-lives approaching 150 ms [43]. Carrying out these measurements required the use of ω_c excitations as brief as 50 ms and ω_+ cleaning excitations as long as 300 ms in certain cases.

As discussed in section 3.3.1, the main limiting factor of the ToF-ICR method is the cycle time required for a measurement of sufficient precision to be completed. The closer a contaminant is in frequency to the species under examination, the longer the cleaning excitation must be in order to remove a contaminant without disturbing the desired species. The end result is that the quadrupole excitation, and the resolution by extension, is constrained by the length of the required cleaning excitation and the life-time of the species under examination. This is problematic when the target species is short-lived and contaminants are present. With fission yields at the level of 10^{-4} and lower, contaminant ions are often present at levels greater than the ^{252}Cf fission fragments.

While the installation of the stronger 1.7Ci ^{252}Cf source was meant to provide a higher yield of the low branches, this has not been fully realized as the source was made too thick [53]. Prior to the upgrades to CARIBU and the CPT, we had reached the limit of what we could measure. The remaining option in order to push out further from stability was to reduce the time requirement for a precision measurement. This has been accomplished through the introduction of the PI-ICR measurement technique at the CPT.

The greatest reduction in the measurement cycle time comes from the removal of the previously necessary ω_+ cleaning excitation. The MR-ToF will provide additional high resolution mass separation on a timescale of tens of milliseconds if cleaning of contaminants is required for a measurement, an order of magnitude lower than the duration of a typical ω_+ cleaning excitation (see section 3.1.5).

Further reduction in the measurement cycle time comes from the duration of the phase accumulation time in comparison to the length of the quadrupolar excitation in ToF-ICR measurements. With a ToF-ICR measurement, an excitation on the order of hundreds of milliseconds is required to obtain a precision of 10^{-7}. As shown in tables A.1 and A.2, the majority of the PI-ICR measurements in this work had phase accumulation times of less than 100 ms and as low as 13 ms while still producing results with the same level of precision.

With these improvements to the experiment, we are now able to push further out from stability than previously possible. As highlighted in fig. 4.6, a large range of new species are now accessible for measurement. Among the species now believed to be in reach are several influential nuclei highlighted in r process sensitivity studies [54]. Since many of the masses of these nuclei have yet to be measured experimentally, measurements to a precision of 10^{-7} would be a significant contribution to r process studies.

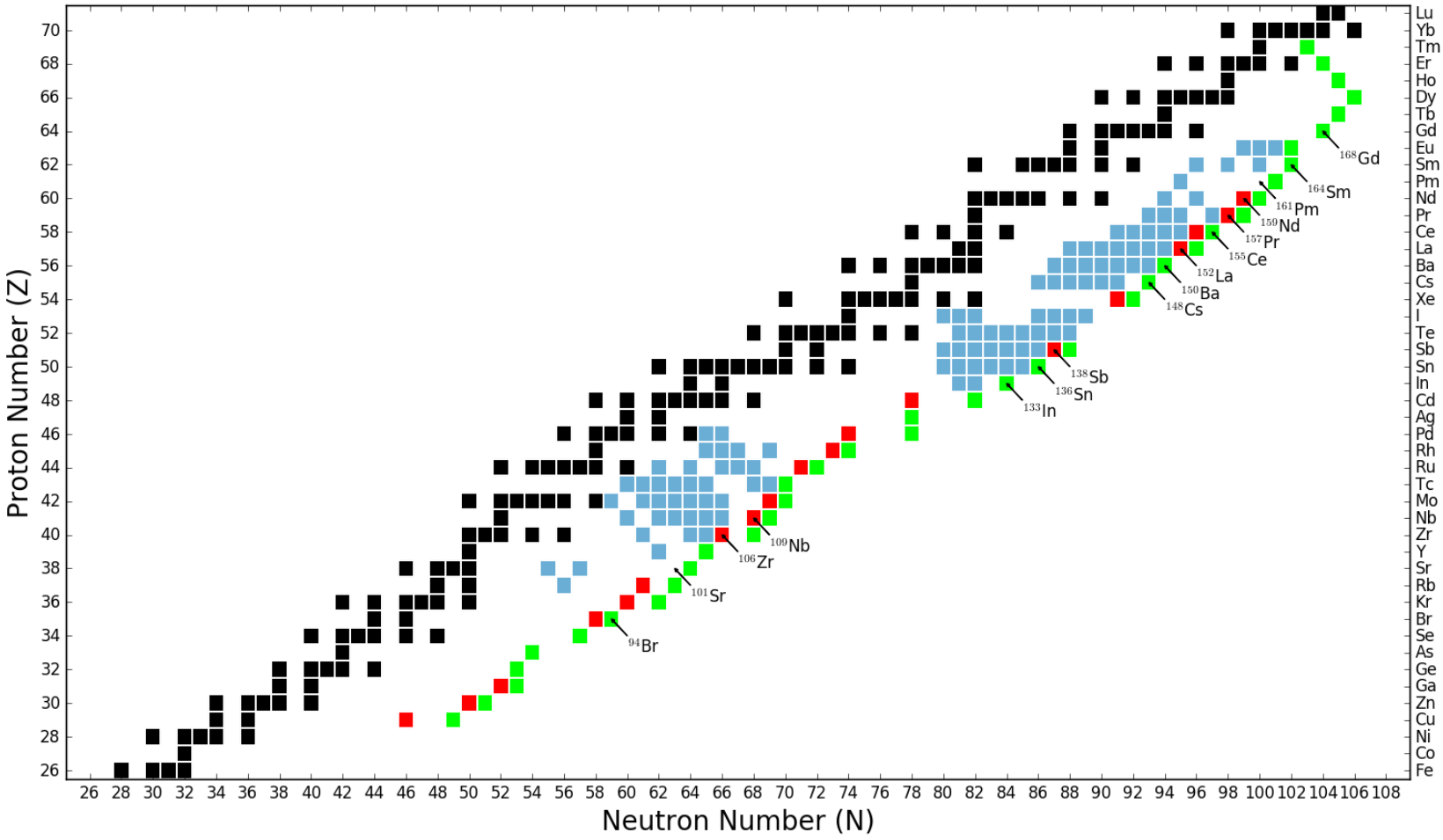

Figure 4.6: The expected range of PI-ICR measurements compared to ToF-ICR at the CPT overlaid on the chart of the nuclides. How neutron rich we expect to be able to push out with PI-ICR is highlighted in green. The limit of ToF-ICR at the CPT is shown in red. Previous CPT measurements are coloured blue. The labeled nuclei have been determined to be of particular astrophysical significance via r process sensitivity studies [54] and have been proposed for measurement [55].

A Appendix

A.1 Excitation Scheme Derivation

Scheme for the reference image:

The phase accumulated by the ions in the time t_1 following the ω_+ excitation is

$$\phi_{1_+} = 2\pi(t_1\nu_+ - N_{1_+}) \tag{A.1}$$

while the phase accumulated by the ions in the time t_2 following the ω_c excitation is

$$\phi_{1_-} = 2\pi(-t_2\nu_- - N_{1_-}) \tag{A.2}$$

Therefore the total phase accumulated over the excitation to produce the reference image is

$$\phi_1 = \phi_{1_+} + \phi_{1_-} = 2\pi[t_1\nu_+ - t_2\nu_- - N_{1_+} - N_{1_-}] \tag{A.3}$$

Scheme for the final image:

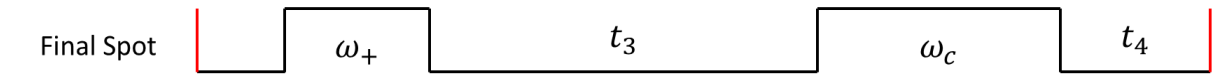

For the final image, the phase accumulated follows the same form as eq. A.3 for the reference

image with the times t_3 and t_4 used in place of t_1 and t_2.

$$\phi_2 = \phi_{2_+} + \phi_{2_-} = 2\pi[t_3\nu_+ - t_4\nu_- - N_{2_+} - N_{2_-}] \tag{A.4}$$

The total phase accumulation between the reference and final images is the difference between the phases ϕ_2 and ϕ_1.

$$\begin{aligned} \Delta\phi &= \phi_2 - \phi_1 \\ &= 2\pi[\nu_+(t_3 - t_1) + \nu_-(t_2 - t_4) - (N_{2_+} + N_{2_-} - N_{1_+} - N_{1_-})] \end{aligned} \tag{A.5}$$

If the times are fixed such that $(t_3 - t_1) = (t_2 - t_4) = t$, then eq. A.5 becomes

$$\begin{aligned} \Delta\phi &= 2\pi[t(\nu_+ + \nu_-) - (N_{2_+} + N_{2_-} - N_{1_+} - N_{1_-})] \\ &= 2\pi[t\nu_c - (N_+ + N_-)] \end{aligned} \tag{A.6}$$

which is eq. 2.48.

A.2 Independent PI-ICR Measurements for $^{133}Cs^{+}$

Date	Frequency (Hz)	Delay Time (ms)
June 12th	657 844.452(22)	65
June 12th	657 844.371(16)	68
June 12th	657 844.597(11)	150
June 12th	657 844.3635(63)	164
June 12th	657 844.4085(42)	215
June 12th	657 844.6020(78)	216
June 19th	657 844.848(57)	28
June 19th	657 844.338(19)	81
June 19th	657 844.285(17)	96
June 19th	657 844.875(15)	109
June 19th	657 844.4341(76)	200
June 22nd	657 844.097(46)	32
June 22nd	657 844.520(34)	50
June 22nd	657 844.538(18)	66
June 22nd	657 844.299(14)	66
June 22nd	657 844.507(14)	66
June 22nd	657 844.086(23)	73
June 22nd	657 844.671(17)	90
June 22nd	657 844.5361(83)	201
June 22nd	657 844.4340(83)	207

Table A.1: Frequencies of $^{133}Cs^{+}$ measured using the PI-ICR method and their corresponding delay times.

A.3 Independent PI-ICR Measurements from CARIBU

Species	Date	Frequency (Hz)	Delay Time (ms)
$^{142}Cs^{+}$	June 11th	616 040.707(23)	66
$^{142}Cs^{+}$	June 11th	616 040.558(13)	116
$^{142}Cs^{+}$	June 11th	616 040.408(10)	184.3
$^{142}Cs^{+}$	June 16th	616 040.135(25)	50
$^{142}Cs^{+}$	June 16th	616 040.139(26)	50
$^{142}Cs^{+}$	June 16th	616 040.496(24)	73
$^{142}Cs^{+}$	June 16th	616 040.312(23)	73
$^{142}Cs^{+}$	June 17th	616 040.819(17)	66
$^{142}Cs^{+}$	June 17th	616 040.126(17)	66
$^{142}Cs^{+}$	June 17th	616 040.375(13)	66
$^{142}Xe^{+}$	June 11th	616 016.136(36)	66
$^{142}Xe^{+}$	June 11th	616 015.824(24)	116
$^{142}Xe^{+}$	June 11th	616 015.045(13)	184.3
$^{142}Xe^{+}$	June 16th	616 015.658(26)	50
$^{142}Xe^{+}$	June 16th	616 015.396(25)	50
$^{142}Xe^{+}$	June 16th	616 015.890(21)	73
$^{142}Xe^{+}$	June 16th	616 015.710(20)	73
$^{142}Xe^{+}$	June 17th	616 015.783(53)	66
$^{142}Xe^{+}$	June 17th	616 016.041(31)	66
$^{142}Xe^{+}$	June 17th	616 015.601(15)	66
$^{143}Cs^{+}$	June 15th	611 717.356(55)	60
$^{143}Cs^{+}$	June 15th	611 717.038(30)	135
$^{143}Cs^{+}$	June 16th	611 716.888(18)	90
$^{143}Cs^{+}$	June 16th	611 716.976(14)	90
$^{143}Cs^{+}$	June 16th	611 717.101(16)	90
$^{143}Cs^{+}$	June 16th	611 717.9262(95)	201
$^{143}Cs^{+}$	June 16th	611 717.1770(74)	201
$^{143}Cs^{+}$	June 16th	611 717.0841(66)	201
$^{144}Cs^{+}$	June 16th	607 446.9188(19)	207
$^{146}Cs^{+}$	June 16th	599 086.604(19)	129
$^{146}Cs^{+}$	July 17th	599 086.680(88)	13
$^{146}Cs^{+}$	July 17th	599 086.908(36)	39
$^{146}Cs^{+}$	July 17th	599 087.020(30)	54
$^{146}Cs^{+}$	July 17th	599 086.406(38)	66

Table A.2: Frequencies of species from CARIBU measured using the PI-ICR method and their corresponding delay times.

References

[1] J. R. Pierce. *Theory and Design of Electron Beams* D. van Nostrand Co., New York, 1949.

[2] H.-Jürgen Kluge. Penning trap mass spectrometry of radionuclides. *International Journal of Mass Spectrometry*, vol. 349-350, pp. 26-37, 2013.

[3] Hans Dehmelt. Experiments with an isolated subatomic particle at rest. *Review of Modern Physics*, vol. 62, pp. 525-530, 1990.

[4] G. Gärtner and E. Klempt. A Direct Determination of the Proton-Electron Mass Ratio. *Zeitschrift für Physik A*, Vol. 287, pp.1-6, 1978.

[5] G.Bollen, P. Dabkiewicz, P. Egelhof, T. Hilberath, H.Kalinowsky, F. Kern, H. Schnatz, L. Schweikhard, H. Stolzenberg, R.B. Moore, H.-J. Kluge, G.M. Temmer, and G. Ulm. First absolute mass measurements of short-lived isotopes. *Hyperfine Interactions*, vol. 38, pp. 793-802, 1987.

[6] Klaus Blaum. High-accuracy mass spectrometry with stored ions. *Physics Reports*, vol. 425, pp. 1-78, 2006.

[7] J. Van Schelt, D. Lascar, G. Savard, J.A. Clark, P.F. Bertone, S. Caldwell, A. Chaudhuri, J. Fallis, J. P. Greene, A.F. Levand, G. Li, K.S. Sharma, M.G. Sternberg, T. Sun, and B.J. Zabransky. Mass measurements near the r process path using the Canadian Penning Trap mass spectrometer. *Physical Review C*, 85:045805, April 2012.

[8] J. Van Schelt, D. Lascar, G. Savard, J.A. Clark, P.F. Bertone, S. Caldwell, A. Chaudhuri, A.F. Levand, G. Li, G.E. Morgan, R. Orford, R.E. Segel, K.S. Sharma, and M.G. Sternberg. First results from the CARIBU facility: Mass measurements on the r process path. *Physical Review Letters*, 111:061102, August 2013.

[9] Brian D. Fields and Keith A. Olive. Big bang nucleosynthesis. *Nuclear Physics A*, vol. 777, pp. 208-225, 2004.

[10] E. Margaret Burbridge, G. R. Burbridge, William A. Fowler, and F. Hoyle. Synthesis of the Elements in Stars. *Reviews of Modern Physics*, vol. 29, pp. 547-650, 1957.

[11] M. Arnould, S. Goriely, and K. Takahashi. The r process of stellar nucleosynthesis: Astrophysics and nuclear physics achievements and mysteries. *Physics Reports*, vol. 450, pp.97-213, 2007.

[12] Yong-Zhong Qian. The Origin of the Heavy Elements: Recent Progess in the Understanding of the r process. *Progress in Particle and Nuclear Physics*, vol. 50, pp. 153-199, Jan. 2003.

[13] S. Goriely and M. Arnould. The r process in the light of a microscopic model for nuclear masses. *Astronomy and Astrophysics*, vol. 262, pp. 73, 1992.

[14] M. Wang, G. Audi, A.H. Wapstra, F.G. Kondev, M. MacCormick, X. Xu, and B. Pfeiffer. The AME2012 atomic mass evaluation. *Chinese Physics C*, vol. 36, pp. 1603-2014, 2012.

[15] R. Surman, J. Beun, G.C. McLauglin, and W.R. Hix. neutron-capture rates near $A = 130$ that effect a global change to the r process abundance distribution. *Physical Review C*, vol. 79, 045809, 2009.

[16] Matthew R. Mumpower and G.C. McLaughlin. Formation of the rare-earth peak: Gaining insight into late-time r process dynamics. *Physical Review C*, vol. 85, 04581, 2012.

[17] Matthew R. Mumpower, G.C. McLaughlin, and Rebecca Surman. The rare earth peak: An overlooked r process diagnostic. *The Astrophysical Journal*, vol. 752, pp. 117, 2012.

[18] J. Duflo and A.P. Zuker. Microscopic mass formulas. *Physical Review C*, vol. 52:R23, 1995.

[19] Hiroyuki Koura, Takahiro Tachibana, Masahiro Uno, and Masami Yamada. Nuclidic mass formula on a spherical basis with an improved even-odd term. *Progress of Theoretical Physics*, vol. 113, pp. 305-325, 2005.

[20] Y. Aboussir, J.M. Pearson, A.K. Dutta, and F. Tondeur. Nuclear mass formula via an approximation to the Hartree-Fock method. *Atomic Data and Nuclear Data Tables*, vol. 61, pp. 127-176, 1995.

[21] Min Liu, Ning Wang, Yangge Deng, and Xizhen Wu. Further improvements on a global nuclear mass model. *Physical Review C*, vol. 84, 014333, 2011.

[22] S. Goriely, N. Chamel, and J.M. Pearson. Further explorations of Skyrme-Hartree-Fock-Bogoliubov mass formulas. XIII. The 2012 atomic mass evaluation and the symmetry coefficient. *Physical Review C*, vol. 88, 024308, 2013.

[23] P. Moller, J.R. Nix, W.D. Myers, and W.J. Swiatecki. Nuclear ground-state masses and deformations. *Atomic Data and Nuclear Data Tables*, vol. 59, pp. 185-381, 1995.

[24] P.H. Dawson (Ed.). Quadrupole Mass Spectrometry and its Applications. Elsevier, Amsterdam, 1976.

[25] W. Paul. Electomagnetic traps for charged and neutral particles. *Reviews of Modern Physics*, vol. 62. pp.531-540, 1990.

[26] G. Li. *Electron-Neutrino Angular Correlation Measurement in the Decay of* ^{8}*Li*. PhD thesis, McGill University, 2012.

[27] Lowell S. Brown and Gerald Gabrielse. Geonium theory: Physics of a single electron or ion in a Penning trap. *Reviews of Modern Physics*, vol. 58, pp. 233-311, 1986.

[28] K. Blaum, G. Bollen, F. Herfurth, A. Kellerbauer, H-J. Kluge, M. Kuckein, S. Heinz, P. Schmidt, and L. Schwelkhard. Recent developments at ISOLTRAP: towards a relative mass accuracy of exotic nuclei below 10^{-8}. *Journal of Physics B: Atomic, Molecular and Optical Physics*, vol. 36, pp. 921-930, 2003.

[29] M. König, G. Bollen, H-J. Kluge, T. Otto, and J. Szerypo. Quadrupole excitation of stored ion motion at the true cyclotron frequency. *International Journal of Mass Spectrometry and Ion Processes*, vol. 142, pp. 95-116, 1995.

[30] S. Eliseev, K. Blaum, M. Block, A. Dörr, C. Droese, T. Eronen, M. Goncharov, M. Höcker, E. Minaya Ramirez, J. Ketter, D.A. Nesterenko, Yu. N. Novikov, and L. Schweikhard. A phase-imaging technique for cyclotron-frequency measurements. *Applied Physics B*, vol. 114, pp. 107-128, 2013.

[31] M. Goncharov. *High-precision Penning-trap mass spectrometry at SHIPTRAP and PENTATRAP for neutrino physics research*. PhD thesis, Heidelberg University, 2014.

[32] J. Van Schelt. *Precision Mass Measurements of Neutron-Rich Nuclei, and Limitations on the r-Process Environment*. PhD thesis, The University of Chicago, 2012.

[33] Daniel Lascar. *Precision Mass Measurements of Short-Lived, Neutron-Rich, R-Process Nuclei About the N=82 Waiting Point*. PhD thesis, Northwestern University, 2012.

[34] N. Nica. Nuclear Data Sheets for A=252. *Nuclear Data Sheets*, vol. 106, pp. 813-834, 2005.

[35] T. R. England and B. F. Rider. Evaluation and Compilation of Fission Product Yields. Los Alamos National Laboratory, October 1994.

[36] G. Savard, J. Clark, C. Boudreau, F. Buchinger, J.E. Crawford, H. Geissel, J.P. Greene, S. Gulick, A. Heinz, J.K.P. Lee, A. Levand, M. Maier, G. Münzenberg, C. Scheiden-

berger, D. Seweryniak, K.S. Sharma, G. Sprouse, J. Vaz, J.C. Wang, B.J. Zabransky, and Z. Zhou. Development and operation of gas catchers to thermalize fusion-evaporation and fragmentation products. *Nuclear Instruments and Methods in Physics Research Section B: Beam Interactions with Materials and Atoms*, vol. 204, pp. 582-586, 2003.

[37] R.N. Wolf. *First on-line applications of a multi-reflection time-of-flight mass separator at ISOLTRAP and the mass measurement of* ^{82}*Zn*. PhD thesis, University of Greifswald, 2013.

[38] Wolfgang R. Plaß, Timo Dickel, Ulrich Czok, Hans Geissel, Martin Petrick, Katrin Reinheimer, Christoph Scheidenberger, and Mikhail I. Yavor. Isobar separation by time-of-flight mass spectrometry for low-energy radioactive ion beam facilities. *Nuclear Instruments and Methods in Physics Research B*, vol. 266, pp. 4560-4564, 2008.

[39] R.N. Wolf, D. Beck, K. Blaum, Ch. Böhm, Ch. Borgmann, M. Breitenfeldt, F. Herfurth, A. Herlert, M. Kowalska, S. Kreim, D. Lunny, S. Naimi, D. Neidherr, M. Rosenbusch, L. Schweikhard, J. Stanja, F. Wienholtz, and K. Zuber. On-line separation of short-lived nuclei by a multi-reflection time-of-flight device. *Nuclear Instruments and Methods in Physics Research A*, vol. 686, pp.82-90, 2012.

[40] Jennifer Fallis. *The Masses of Proton-Rich Isotopes of Nb, Mo, Tc, Ru and Rh and Their Influence on the Astrophysical rp and vp Processes*. PhD thesis, University of Manitoba, 2009.

[41] RoentDek Handels Gmbh. *MCP delay line Detector Manual* Roentdek.

[42] S. George, K. Blaum, M. Block, M. Breitenfeldt, M. Dworschak, F. Herfurth, A. Herlert, M. Kowalska, M. Kretzschmar, E. Minaya Ramirez, D. Neidherr, S. Schwarz, and L.

Schweikhard. Damping effects in Penning trap mass spectrometry. *International Journal of Mass Spectrometry*, vol. 299, pp. 102-112, 2011.

[43] Rodney Orford. *Precision mass measurements of neutron-rich rare isotopes approaching the r-process path with the Canadian Penning Trap mass spectrometer*. MSc. thesis, McGill University, 2014.

[44] G. Bollen. Mass measurements of short-lived nuclides with ion traps. *Nuclear Physics A*, vol. 693, pp. 3-18, 2001.

[45] D. Neidherr, R. B. Cakirli, G. Audi, D. Beck, K. Blaum, Ch. B$'$ohm, M. Breitenfeldt, R. F. Casten, S. George, F. Herfurth, A. Herlert, A. Kellerbauer, M. Kowalska, D. Lunney, E. Minaya-Ramirez, S. Naimi, M. Rosenbusch, S. Schwarz, and L. Schweikhard. *Physical Review C*, vol. 80, 044323, 2009.

[46] M. Przewloka, A. Przewloka, P. Wächter, and H. Wollnik. *Zeitschrift für Physik A*, vol. 342, pp.27-29, 1992.

[47] M. Graefenstedt, U. Keyser, F. Münnich, and F. Schreiber *Proc. 5th Int. Conf. Nuclei far from Stability.* AIP Conf. Proc. 164, pp.30-40, 1988.

[48] R. Decker, K.D. Wünsch, H. Wollnil, G. Jung, and J. Münzel. *Zeitschrift für Physik A*, Vol. 301, pp.165-175, 1981.

[49] T.D. Johnson, D. Symochko, M. Fadil, and J.K. Tuli. Nuclear Data Sheets for A=142. *Nuclear Data Sheets*, vol. 112, pp.1949-2127, 2011.

[50] E. Browne and J.K. Tuli. Nuclear Data Sheets for A=143. *Nuclear Data Sheets*, vol. 113, pp. 715-908, 2012.

[51] A.A. Sonzogni. Nuclear Data Sheets for A=144. *Nuclear Data Sheets*, vol. 93, pp. 599-762, 2001.

[52] L.K. Peker and J.K. Tuli. Nuclear Data Sheets for A=146. *Nuclear Data Sheets*, vol. 82, pp. 187-378, 1997.

[53] G. Savard. Private communication. 2015.

[54] S. Brett, I. Bentley, N. Paul, R. Surman, and A. Aprahamian. Sensitivity of the r process to nuclear masses. *The European Physical Journal A*, vol. 48, article 184, 2012.

[55] N. Paul et. al. *Mass Measurements of Neutron-rich Nuclei Influential to r-Process Abundances.* Measurement proposal, The University of Notre Dame, 2012.